

# Coupled 1D Chemical Kinetic-Transport and 2D Hydrodynamic Modeling Supports a modest 1–1.5× Supersolar Oxygen Abundance in Jupiter’s Atmosphere

JEEHYUN YANG ,<sup>1, 2, 3</sup> ALI HYDER ,<sup>1</sup> RENYU HU ,<sup>1, 4, 5, 6</sup> AND JONATHAN I. LUNINE ,<sup>1, 2</sup>

<sup>1</sup>*Jet Propulsion Laboratory, California Institute of Technology, Pasadena, CA 91109, USA*

<sup>2</sup>*Division of Geological and Planetary Sciences, California Institute of Technology, Pasadena, CA 91125, USA*

<sup>3</sup>*Department of Astronomy and Astrophysics, The University of Chicago, Chicago, IL 60637, USA*

<sup>4</sup>*Department of Astronomy & Astrophysics, The Pennsylvania State University, University Park, PA 16802, USA*

<sup>5</sup>*Center for Exoplanets and Habitable Worlds, The Pennsylvania State University, University Park, PA 16802, USA*

<sup>6</sup>*Institute for Computational and Data Science, The Pennsylvania State University, University Park, PA 16802, USA*

## ABSTRACT

Understanding the deep atmospheric composition of Jupiter provides critical constraints on its formation and the chemical evolution of the solar nebula. In this study, we combine one-dimensional thermochemical kinetic-transport modeling with two-dimensional hydrodynamic simulations to constrain Jupiter’s deep oxygen abundance using carbon monoxide (CO) as a proxy tracer. Leveraging a comprehensive chemical network generated by Reaction Mechanism Generator (RMG), we assess the impact of updated reaction rates, including the often-neglected but thermochemically significant Hidaka reaction ( $\text{CH}_3\text{OH} + \text{H} \rightarrow \text{CH}_3 + \text{H}_2\text{O}$ ). Our 1D-2D coupled approach supports a modest supersolar oxygen enrichment of 1.0–1.5× the solar value. We also present a method for deriving Jupiter’s eddy diffusion coefficient ( $K_{zz} = 3 \times 10^6$  to  $5 \times 10^7 \text{ cm}^2/\text{s}$ ) from 2D hydrodynamic simulations using the quasi steady-state approach. This method is applicable to exoplanet atmospheres, where  $K_{zz}$  remains highly uncertain despite its strong influence on atmospheric chemistry. Finally, our results imply a significantly elevated planetary carbon-to-oxygen (C/O) ratio of ∼2.9, highlighting the importance of clarifying the mechanisms behind the preferential accretion of carbon-rich material during Jupiter’s formation. By integrating thermochemical and hydrodynamic processes, our study offers a more complete framework for constraining chemical and dynamical processes in (exo)planetary atmospheres.

*Keywords:* Jupiter (873), Planet formation (1241), Planetary atmospheres (1244), Proto-planetary disks (1300)

## 1. INTRODUCTION

Understanding the composition of giant planets is key to constraining their formation mechanisms. In particular, the abundances of carbon and oxygen provide insight into where a planet formed within the protoplanetary disk, as well as its accretion history and subsequent evolution (Öberg et al. 2011; Mousis et al. 2019). For this reason, measuring species such as water, methane, and ammonia, and characterizing the chemistry of Jupiter’s deep atmosphere (as probed by the Galileo and Juno missions), has been a major focus in planetary science

(Niemann et al. 1998; Bézard et al. 2002; Wong et al. 2004; Bjoraker et al. 2018). Among these, determining the oxygen abundance in Jupiter’s deep atmosphere remains particularly challenging since water, the primary oxygen-bearing species, undergoes condensation and complex hydrodynamic processes, often resulting in locally depleted abundances and complicating efforts to measure a representative mixing ratio for the entire envelope. Instead, carbon monoxide, which is physically and chemically stable under Jupiter’s deep atmospheric conditions and thus readily detectable, is frequently used as a proxy to constrain the deep oxygen abundance through one-dimensional (1D) chemical kinetic-transport models (Prinn & Barshay 1977;

Visscher et al. 2010; Wang et al. 2015, 2016; Cavalié et al. 2023).

Recently, Cavalié et al. (2023) reported a subsolar oxygen abundance of 0.3 times the protosolar value using a 1D chemical kinetic-transport model that incorporated an updated chemical network from Venot et al. (2020) (hereafter referred to as V20) and assumed an eddy diffusion coefficient ( $K_{zz}$ ) of  $10^8 \text{ cm}^2/\text{s}$ . The chemical network developed by Venot et al. (2020) (i.e., V20) excluded the reaction  $\text{H} + \text{CH}_3\text{OH} \rightarrow \text{CH}_3 + \text{H}_2\text{O}$  (hereafter referred to as the Hidaka reaction), originally derived by Hidaka et al. (1989). While Venot et al. (2020) found that hot Jupiter chemistry is relatively insensitive to the inclusion of this reaction, they showed that it significantly affects CO/CH<sub>4</sub> interconversion in cooler, higher-pressure environments such as warm Neptunes (for example, in GJ 436 b, including the Hidaka reaction led to a  $\sim 2.5 \times$  increase in the quenched CO mole fraction), T dwarfs, and potentially Neptune and Uranus. This, then, raises the question of whether it is appropriate to exclude the Hidaka reaction in modeling Jupiter's atmosphere (Cavalié et al. 2023), given the relatively cool temperatures and high pressures present in its deep atmospheric layers.

In addition to limitations in the chemical network, the 1D kinetic-transport framework simplifies vertical mixing by representing it with a single eddy diffusion coefficient ( $K_{zz}$ ). Although several 1D models include vapor phase change behavior and condensable species, the underlying mixing strength is assumed to be decoupled from these effects and treated independently. In reality, increased condensation near the cloud layers can inhibit mixing by stabilizing the atmosphere against convective instability. As a result, the 1D model's ability to accurately constrain Jupiter's oxygen abundance is limited. To address this limitation, Hyder et al. (2025) used a 2D hydrodynamic modeling framework to simulate atmospheric dynamics at and below the water cloud level. They incorporated simplified CO thermochemistry by using the temperature- and pressure-dependent chemical lifetime of CO to capture the influence of hydrodynamic transport on CO abundance in Jupiter's troposphere. Their results support a supersolar enrichment of Jupiter's deep atmosphere, with metalicities estimated between 2.5 and 5 times solar. However, the CO chemical timescale in Hyder et al. (2025) was obtained by applying a scaling factor to the CO–CH<sub>4</sub> interconversion timescale derived by

Wang et al. (2015), which itself was based on the chemical network of Venot et al. (2012) (hereafter V12). Given that the V12 network has since been substantially updated in Venot et al. (2020) (V20), it would be preferable to empirically derive the CO chemical timescale using the more recent and more comprehensive chemical network to precisely capture CO–CH<sub>4</sub> interconversion and its coupling with hydrodynamic behavior.

Over the past decade, advances in computational chemical engineering, particularly through rate-based algorithms, have enabled more precise and comprehensive predictive chemistry (Gao et al. 2016; Liu et al. 2021b; Johnson et al. 2022). This tool, also known as Reaction Mechanism Generator (RMG), assesses and determines key chemical species and reactions based on iterative simulations of the chemical system of interest, producing objective, user-independent, and more complete networks than those traditionally built by individuals. Notably, RMG has not only been widely used in chemical engineering but has also enabled successful simulations of exoplanet atmospheric chemistry recently by coupling its automated reaction mechanism generation with 1D photochemical kinetic-transport modeling using the EPACRIS framework (Yang & Hu 2024a). This approach has been applied to planets such as WASP-39 b, WASP-80 b, K2-18 b, and TOI-270 d, yielding results that are consistent with the JWST observations (Yang & Hu 2024a,b; Benneke et al. 2024; Hu et al. 2025).

Because CO–CH<sub>4</sub> interconversion in the deep atmospheres of giant planets is primarily driven by thermochemistry and vertical mixing rather than photochemistry, applying a rate-based, RMG-generated chemical network in combination with a two-dimensional hydrodynamic transport model enables accurate characterization of these processes. This approach can help constrain the deep oxygen abundance of Jupiter, and at the same time, can be extended to Neptune and Uranus, whose internal compositions remain poorly understood. This is a well-recognized problem in planetary science. For example, the 2020 Planetary Science and Astrobiology Decadal Survey highlights the need for improved understanding of the formation and evolution of the ice giants (National Academies of Sciences, Engineering, and Medicine 2023).

Given this background, in this work we employ both a 2D hydrodynamic model to simulate atmospheric microphysics and vertical transport, and an automated, pressure- and temperature-dependent

chemical network generator to capture complex thermochemical kinetics across a wide range of conditions. By leveraging these two state-of-the-art computational tools, we aim to simulate CO–CH<sub>4</sub> interconversion in Jupiter’s deep troposphere with unprecedented detail and thereby place tighter constraints on its deep oxygen abundance, a key tracer of giant planet formation.

## 2. METHODS

### 2.1. Oxygen and Other Elemental Parameterization of Jupiter’s Tropospheres

To investigate the various oxygen abundance scenarios in Jupiter’s troposphere, we first constrained the abundances of helium (He), carbon (C), nitrogen (N), and sulfur (S) using the values from Table 2 in Wang et al. (2016): [He]/[H<sub>2</sub>] = 0.157, and thus [He]/[H]  $\sim \frac{1}{2}$ [He]/[H<sub>2</sub>] =  $7.85 \times 10^{-2}$ ; [CH<sub>4</sub>]/[H<sub>2</sub>] =  $2.37 \times 10^{-3}$ , and thus [C]/[H]  $\sim \frac{1}{2}$ [CH<sub>4</sub>]/[H<sub>2</sub>] =  $1.19 \times 10^{-3}$ ; [NH<sub>3</sub>]/[H<sub>2</sub>] =  $6.64 \times 10^{-4}$ , and thus [N]/[H]  $\sim \frac{1}{2}$ [NH<sub>3</sub>]/[H<sub>2</sub>] =  $3.32 \times 10^{-4}$ ; [H<sub>2</sub>S]/[H<sub>2</sub>] =  $8.90 \times 10^{-5}$ , and thus [S]/[H]  $\sim \frac{1}{2}$ [H<sub>2</sub>S]/[H<sub>2</sub>] =  $4.45 \times 10^{-5}$ . These values are based on Galileo Probe Mass Spectrometer (GPMS) measurements of the major gas species’ mixing ratios relative to H<sub>2</sub> (Niemann et al. 1998; Wong et al. 2004). Next, we adopted an astronomical log-scale abundance,  $A(E)$ , using a value of 8.73 for oxygen, corresponding to the present-day solar oxygen abundance from Table 3 of Lodders (2021). We set this oxygen abundance as O/H=1× $Z_{\odot}$ , where  $Z_{\odot}$  refers to the solar metallicity. For example, if the oxygen enrichment factor  $E$  is 2.3, then the O/H ratio is given by  $10^{8.73+\log_{10}2.3-12} \sim 1.24 \times 10^{-3}$ . Finally, we derived the elemental abundances by normalizing the sum of H, He, C, N, O, and S to unity, and the resulting elemental composition profiles for each O/H enrichment scenario are listed in Table A 1. It has to be noted that since we adopted the carbon abundance constrained by the GPMS measurement, the resulting carbon-to-oxygen ratio (C/O) for the O/H=1× $Z_{\odot}$  scenario is 2.21, which is significantly higher than the present-day solar C/O = 0.55 (Lodders 2021) (corresponding to  $\sim 4\times$  the solar C/O using values from Lodders (2021) and  $\sim 4.4\times$  using Asplund et al. (2009)). Within this framework, the H<sub>2</sub>O abundance ( $2.5 \times 10^3$  ppm) inferred for Jupiter’s equatorial region by the Juno Microwave Radiometer (MWR) measurements in 2020 (Li et al. 2020) corresponds to O/H =  $2.7^{+2.4}_{-1.7} \times Z_{\odot}$  and C/O =  $0.82^{+0.39}_{-1.39}$ , and the latest analysis of

the O/H ratio from Juno data by Li et al. (2024) corresponds to O/H =  $4.5 \pm 3.1 \times Z_{\odot}$  (It has to be noted that Li et al. (2024) adopted the  $A(E)$  value from Asplund et al. (2009), and reported O/H =  $4.9 \pm 3.4 \times Z_{\odot}$ ).

### 2.2. The $T$ - $P$ and $K_{zz}$ profiles for Jupiter’s Tropospheres

The temperature–pressure ( $T$ – $P$ ) profile of Jupiter is adopted from Seiff et al. (1998); Simon-Miller et al. (2006). The vertical eddy diffusion coefficient ( $K_{zz}$ ) is taken from Moses et al. (2005), which was developed to reproduce observed abundances of various atmospheric species (Atreya et al. 1981; Vervack Jr et al. 1995; Yelle et al. 1996; Lara et al. 1998; Edgington et al. 1999; Drossart et al. 1999, 2000; Bézard et al. 2002; Lellouch et al. 2002; Moreno et al. 2003). Since the major purpose of the current study is to investigate the quenching of carbon monoxide in Jupiter’s deep atmosphere ( $P \geq 10$  bar) in detail, we have varied the deep atmospheric  $K_{zz}$  value from  $5 \times 10^6$  to  $10^9$  cm<sup>2</sup> s<sup>-1</sup>, with a nominal value of  $10^8$  cm<sup>2</sup> s<sup>-1</sup> (see black solid line in Figure B1 in Appendix B).

### 2.3. Chemical Networks

The chemical network constructed using the Reaction Mechanism Generator (Gao et al. 2016; Johnson et al. 2022, RMG), a rate-based automatic reaction network generator, has been shown to be applicable under both H<sub>2</sub>-rich and H<sub>2</sub>O-rich atmospheric conditions (Yang & Hu 2024b). Given that Jupiter’s equilibrium temperature falls within the range observed for temperate sub-Neptunes and considering its H<sub>2</sub>-dominated atmosphere and potentially water-rich interior, we adopted the chemical reaction network from Yang & Hu (2024b) to perform one-dimensional thermochemical kinetic-transport modeling of Jupiter’s troposphere. This framework may also be suitable for modeling the atmospheres of Uranus and Neptune. The resulting chemical network includes 89 species involved in 1968 forward–reverse reaction pairs. It is provided as a YAML file (in Cantera format) and is available at: <https://doi.org/10.5281/zenodo.16750016> (Yang 2025). Note that photochemical species and their associated reactions are not considered in the current study and have thus been excluded from the network. The comparison among various chemical networks used in previous 1D modeling studies of Jupiter’s troposphere (Wang et al. 2016; Cavalie et al. 2023) is shown in Figure C2 in Appendix C. In

this study, for our one-dimensional thermochemical kinetic-transport atmospheric modeling (described in Section 2.4), we investigated the effect of the Hidaka reaction on Jupiter’s deep atmospheric oxygen abundance by comparing both the conventional TST-based rate coefficient from Moses et al. (2011) and the *d*-TST-based coefficient from Sanches-Neto et al. (2017). For the two-dimensional hydrodynamic modeling (described in Section 2.5), we used only the rate coefficient reported by Moses et al. (2011).

#### 2.4. 1D Thermochemical Kinetic-transport Atmospheric Modeling—EPACRIS

Based on the various elemental abundance scenarios described in Section 2.1, the  $T$ – $P$  and  $K_{zz}$  profiles of Jupiter’s atmosphere described in Section 1, and the chemical network described in Section 2.3, we performed 1D thermochemical kinetic-transport modeling of Jupiter’s troposphere using the chemistry module of EPACRIS (Yang & Hu 2024a). This model simulates the steady-state vertical mixing ratios of chemical species under different O/H scenarios in Jupiter’s atmosphere. As noted in Section 2.2, the primary goal of this study is to investigate the quenching of carbon monoxide in Jupiter’s deep atmosphere. Accordingly, photochemical reactions are not included in our study. This limits the validity of our results to pressures below at least 4 bars, above the  $\text{H}_2\text{O}$  cloud deck, where ultraviolet photons cannot penetrate (Bjoraker et al. 2018). Since quenching occurs at much deeper levels, this exclusion of photochemistry does not affect our analysis.

#### 2.5. 2D Hydrodynamic Modeling—SNAP

As the distribution of disequilibrium species is affected by cloud layer dynamics and deeper convective processes, we employ the SNAP hydrodynamic model used in Hyder et al. (2025), coupled with our newly constructed CO– $\text{CH}_4$  chemical network generated by RMG (see Section 2.3 for details), to determine vertical distribution of CO in Jupiter’s atmosphere. It employs a non-hydrostatic formulation with active cloud resolving capabilities (Li & Chen 2019), which are crucial in simulating the distribution of trace species in convective and diffusive atmospheres.

The vertical coordinate of our hydrodynamic simulation spans the entire pressure range relevant to the problem, starting near  $\sim 0.3$  and extending down to  $\sim 7 \times 10^3$  bars (a vertical distance of

525 km) with  $\Delta z \sim 2$  km, encapsulating the water lifting condensation level (LCL) and the CO quench region in the deep atmosphere. The Jovian scale height,  $H \sim 40$  km, is well-resolved with this specification. The horizontal resolution is kept lower to limit the computational cost of the simulations with  $\Delta x \sim 4$  km and spans 1200 km, corresponding to about  $1^\circ$  on Jupiter. Similar to Hyder et al. (2025), we allow for top cooling without bottom heating; the difference is only in the rate of numerical convergence and does not affect the results presented here. As the horizontal extent is small relative to the characteristic scale of Jupiter’s zonal jets, large-scale latitudinal trends are ignored. This means that our results are primarily applicable to the equatorial region of Jupiter, although trace species have been observed to vary significantly in latitude (Grassi et al. 2020). While our model is equatorially focused, the observational CO data used in this study include both equatorial and midlatitude measurements, consistent with Earth-based viewing geometries. Specifically, the original Bézard et al. (2002) measurement was taken from  $6 - 12^\circ\text{N}$ , while more recent observations from Bjoraker et al. (2018) targeted the Great Red Spot, located near  $20^\circ\text{S}$ . The combined results from both studies were used to establish the observational range shown as the cross-hairs in Figure 5. We apply a reflective and periodic boundary for the vertical and horizontal coordinates, respectively, with homogeneous cooling employed at the top boundary, identical to the setup in Hyder et al. (2025).

The simulations are evolved till the rate of change of the mean CO mole fraction,  $\partial \langle X_{\text{CO}} \rangle / \partial t$ , in the top 20 bars of the atmosphere stabilizes to  $\sim 0$ . This occurs when this value falls below machine precision ( $10^{-16}$ ) (Figure E5), indicating a statistical steady state between the thermochemical production/loss terms and the vertical turbulent transport. We focus on the top 20 bars because this region encompasses the upper atmosphere where the mean vertical tracer gradient varies significantly, particularly near the water cloud deck, which lies between 5 and 10 bars depending on the O/H enrichment. The tracer gradient remains non-zero in this region, ensuring that any variability in tracer transport is fully captured in the average advection rate. The primary equations of motion that are solved in our model are the Euler equations, which are detailed by Li & Chen (2019) along with their numerical treatment and not repeated here.

## 2.6. Deriving empirical $\tau_{\text{chem}}(T, P)$ for use in the SNAP-2D hydrodynamic modeling

Due to the stiffness and computational expense of the system, it is not yet feasible to fully couple chemical reaction kinetics with hydrodynamic modeling described in Section 2.5. Therefore, it is essential to derive the chemical timescale as a function of pressure ( $P$ ) and temperature ( $T$ ) for use in the SNAP-2D hydrodynamical modeling (Section 2.5). For consistency and easier comparison, we followed the procedure described by Wang et al. (2015) and fit the chemical timescale for carbon monoxide using the following fitting formula:

$$\tau_{\text{chem}}(T, P) \sim \alpha \cdot \exp\left(\frac{\beta}{T}\right) \cdot P^\gamma \text{ [s]} \quad (1)$$

where  $T$  and  $P$  represent temperature [K] and pressure [bar], respectively, and  $\alpha$ ,  $\beta$ , and  $\gamma$  are fitted coefficients. It should be noted that this parameterization for estimating the chemical timescale of CO is similar to the approach used by Zahnle & Marley (2014), enabling more accurate predictions of CO quenching across a wide range of conditions while still capturing the overall behavior of the full chemical network.

The fitting was applied to 10 datasets spanning a broad range of O/H = 0.3–7× and  $K_{zz} = 5 \times 10^6$ – $10^9$  [cm<sup>2</sup>/s]. The conditions for each dataset are summarized in Table C2 in Appendix D. Figure C3 in Appendix D shows the comparison between the 10 datasets and the fitted points, the residuals after fitting, and the comparison between the chemical timescale derived by Wang et al. (2015) (V12, redline) and the timescale fitted in this work using the RMG-generated network (Yang & Hu 2024b) (green line). The fitted coefficients  $\alpha$ ,  $\beta$ , and  $\gamma$  for  $\tau_{\text{chem}}(T, P)$  plugged into the SNAP-2D hydrodynamic modeling in this study are:

$$\begin{aligned} \alpha &= 2.89 \times 10^{-12} \\ \beta &= 41889.08 \\ \gamma &= -4.93 \times 10^{-7} \end{aligned}$$

## 2.7. Chemical timescale approach approximation

For comparison, we also show chemical timescale approaches using two distinct RMG-generated chemical networks: one for hot Jupiter atmospheres (Yang & Hu 2024a) and one for temperate sub-Neptune atmospheres (Yang & Hu 2024b) (see Figure D3). Each chemical timescale was calculated using Cantera’s

`Kinetics.net_production_rates` module (Goodwin et al. 2024) along the  $T$ – $P$  profile described in Section 2.2 to construct the Jacobian matrix of the chemical system. We then computed the eigenvectors and eigenvalues of the Jacobian matrix using `scipy.linalg.eig` (Virtanen et al. 2020) and projected CO onto these eigenmodes. The mode with the largest projection was defined as the chemical timescale of CO,  $\tau'_{\text{chem}}(T, P)$ , where the prime ('') distinguishes it from the empirical timescale derived in the previous Section 2.6 (Recall that the empirical timescale is used in the 2D hydrodynamic modeling discussed in Sections 2.5 and 2.6). Further methodological details are provided in Appendix F.

Previous chemical timescale approaches (e.g., Visscher et al. 2010; Visscher & Moses 2011; Moses et al. 2011; Zahnle & Marley 2014; Wang et al. 2016) first incorporated all carbon reactions in 1D chemical-kinetic transport models, then isolated a single rate-limiting step to examine CO quenching behavior across different atmospheric regimes. While choosing a single reaction may simplify calculations, this assumption can lead to inaccuracies since multiple reactions often proceed at comparable rates, and slight variations in conditions (e.g.,  $T$ ,  $P$ , or chemical compositions) can alter which reaction is rate-limiting. Instead, the chemical timescale is derived directly from the eigenmodes and their corresponding eigenvalues of the Jacobian matrix at thermal equilibrium, explicitly considering all relevant reactions in which CO participates. This comprehensive approach provides more precise and realistic estimates for the quenched CO abundance.

The vertical mixing timescale is given by

$$\tau_{\text{mix}} = \frac{L^2}{K_{zz}}, \quad (2)$$

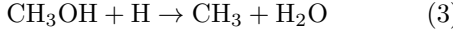
where  $L$  is the characteristic mixing length, and  $K_{zz} = 10^8$  [cm<sup>2</sup>/s] is adopted as a nominal value. We adopt  $L = 0.12H$  (where  $H$  is the pressure and temperature-dependent scale height of Jupiter’s atmosphere), based on mixing length theory (Smith 1998) and previous work on CO quenching kinetics in Jupiter-like atmospheres (Visscher et al. 2010). It should be noted that this parameterization is primarily empirical rather than derived from first principles (Smith 1998). We assume that CO quenches at the level where  $\tau'_{\text{chem}}(T, P) = \tau_{\text{mix}}$ , following the classical timescale comparison approach (Visscher et al. 2010). Figure 4 compares the re-

sulting quench levels for two end-member oxygen abundance scenarios ( $\text{O/H} = 2.3 \times$  and  $0.3 \times Z_{\odot}$ ) using the chemical timescale approach to the outcomes from the EPACRIS–1D modeling results. A detailed discussion is provided in Section 3.2.5.

### 3. RESULTS AND DISCUSSIONS

#### 3.1. Inclusion of the “Hidaka reaction” in the chemical network

The Hidaka reaction refers to the thermal decomposition of methanol by a hydrogen radical:



originally reported by the experimental study of Hidaka et al. (1989). The reaction has been widely studied in the combustion society. The overall reaction  $\text{CH}_3\text{OH} + \text{H}$  proceeds via three primary channels: (1)  $\text{CH}_2\text{OH} + \text{H}_2$ , (2)  $\text{CH}_3\text{O} + \text{H}_2$ , and (3)  $\text{CH}_3 + \text{H}_2\text{O}$ , with the third pathway (the Hidaka reaction) being the most exothermic, as confirmed by ab initio calculations (Lendvay et al. 1997; Sanches-Neto et al. 2017).

This Hidaka reaction has also been incorporated into chemical modeling of various (exo)planetary atmospheres (Visscher et al. 2010; Venot et al. 2012; Wang et al. 2015). However, its inclusion has been a subject of debate. As noted by Visscher et al. (2010) and Moses (2014), the rate coefficient reported by Hidaka et al. (1989) appears anomalously fast relative to its high energy barrier. In response, Moses et al. (2011) recalculated the rate coefficient (referred to as nominal value) using high-level quantum chemical methods (QCISD(T)/CBS//QCISD(T)/cc-pVTZ) and transition state theory with torsional and asymmetric Eckart tunnelling corrections, while others chose to exclude the reaction from their chemical networks (Wang et al. 2016; Venot et al. 2020; Cavalié et al. 2023).

However, two important issues arise regarding how this reaction has been handled in prior works. First, the rate coefficient widely adopted by earlier studies (Visscher et al. 2010; Venot et al. 2012) was based on a misreported value in the NIST database (Manion et al. 2020), rather than the original data from Hidaka et al. (1989). Specifically, the NIST database (as of December 4, 2025) lists the rate coefficient as  $3.32 \times 10^{-10} [\text{cm}^3/\text{molecule/s}] e^{-22.20[\text{kJ/mol}]/\text{RT}}$ , which is two orders of magnitude faster than the actual value reported by Hidaka et al. (1989). The original expression

by Hidaka et al. (1989) is  $2.0 \times 10^{12} [\text{cm}^3/\text{mol/s}] e^{-5.3[\text{kcal/mol}]/\text{RT}}$ . When converted to molecule-based units (i.e., by dividing by Avogadro’s number), the resulting expression becomes  $3.32 \times 10^{-12} [\text{cm}^3/\text{molecule/s}] e^{-22.20[\text{kJ/mol}]/\text{RT}}$ , which is consistent in activation energy (note that 1 cal = 4.184 J) but 100× slower in pre-exponential factor.

As shown in Figure 1, the corrected rate coefficient from Hidaka et al. (1989) is in reasonable agreement with the high-level quantum chemical rate calculated by Moses et al. (2011) within an order of magnitude at temperatures below 1000 K. The discrepancy increases at higher temperatures (above 1000 K), where the Hidaka value becomes approximately more than an order of magnitude slower. This underscores the importance of verifying rate coefficient sources, particularly when extracting values from secondary databases such as the NIST database (Manion et al. 2020). Inaccuracies in pre-exponential factors can have substantial effects on chemical network predictions.

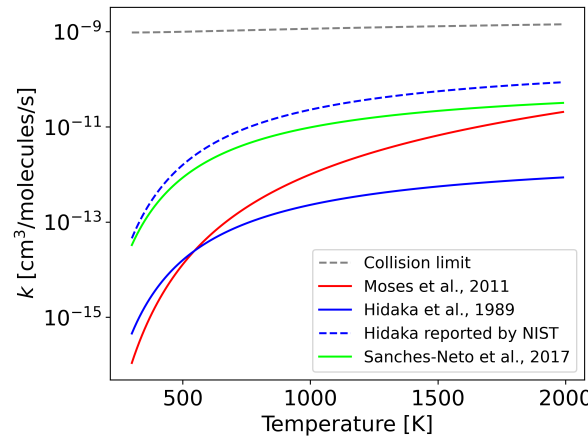


**Figure 1.** The temperature dependence of the rate coefficients for the reaction  $\text{CH}_3\text{OH} + \text{H} \rightarrow \text{CH}_3 + \text{H}_2\text{O}$  from various references. The solid blue line represents the original rate coefficient reported by Hidaka et al. (1989); the blue dashed line corresponds to an incorrect version of this rate listed in the NIST database (Manion et al. 2020); the red solid line shows the rate coefficient calculated by Moses et al. (2011); the lime solid line represents the rate calculated by Sanches-Neto et al. (2017) using the *d*-TST method; and the grey dotted line shows the collision limit calculated using the equation (1) from Chen et al. (2017) for reference.

Another issue regarding the treatment of the Hidaka reaction in prior studies is that some chemical networks have intentionally excluded this reaction from their chemical networks (Venot et al. 2020; Cavalié et al. 2023). This exclusion was typically

justified by the assumption that the competing hydrogen-abstraction channels forming  $\text{CH}_2\text{OH} + \text{H}_2$  and  $\text{CH}_3\text{O} + \text{H}_2$  dominate over the entire temperature range up to 2000 K, as supported by earlier studies (Hoyer et al. 1981; Li & Williams 1996; Kerkeni & Clary 2004; Carvalho et al. 2008; Meana-Pañeda et al. 2011). However, it is important to note that some of these prior works (e.g., Li & Williams 1996) did not consider the  $\text{CH}_3 + \text{H}_2\text{O}$  channel (i.e., the Hidaka channel) in their analyses, and precise experimental measurement of branching ratios for the  $\text{CH}_3\text{OH} + \text{H}$  reaction remains challenging due to the complexity of methanol combustion, which involves numerous competing and side reactions.

Moreover, as shown in Fig. 5 of Sanches-Neto et al. (2017), experimental measurements of the total rate coefficient for the  $\text{CH}_3\text{OH} + \text{H}$  reaction reveal clear deviations from linear Arrhenius behavior at lower temperatures. This sub-Arrhenius curvature is commonly attributed to quantum tunneling effects, which become increasingly significant as temperature decreases (Silva et al. 2013; Carvalho-Silva et al. 2017). These features suggest the need for a more refined theoretical treatment in the moderate tunneling regime. To address this, Sanches-Neto et al. (2017) performed an in-depth assessment of the Hidaka channel using ab-initio *Car-Parrinello* molecular dynamics simulations at two representative temperatures (300 and 2500 K), followed by rate coefficient calculations using high-level *deformed*-transition state theory (hereafter referred to as *d*-TST). This approach offers improved treatment of quantum tunneling compared to conventional transition state theory, which had been used in previous calculations of the Hidaka channel's rate coefficient (Lendvay et al. 1997; Moses et al. 2011). Sanches-Neto et al. (2017) demonstrated that *d*-TST provides a more accurate description of the overall reaction rate constant for the  $\text{CH}_3\text{OH} + \text{H}$  reaction, particularly in the moderate tunneling regime ( $T \leq 1000$  K), compared to previous theoretical approaches (Lendvay et al. 1997; Carvalho et al. 2008; Moses et al. 2011; Meana-Pañeda et al. 2011).

Surprisingly, as shown in Figure 1, the Hidaka reaction rate coefficient calculated using *d*-TST by Sanches-Neto et al. (2017) closely matches the misreported NIST value (lime solid vs. blue dashed line). At higher temperatures, the *d*-TST rate aligns with the conventional TST rate (Moses et al. 2011) indicated by the red solid line, but becomes

up to two orders of magnitude faster at temperatures near 300 K, reflecting significant quantum tunneling. Thus, using the *d*-TST rate in one-dimensional kinetic-transport models lowers the predicted quenched CO mixing ratio due to enhanced CO-to- $\text{CH}_4$  conversion. As shown in Figure B2, models excluding the Hidaka reaction (e.g., V20 or pre-2014 combustion networks) predict CO mixing ratios of  $\sim 4 - 5 \times 10^{-8}$  at 600 K. Including the conventional TST rate lowers this to  $3 - 4 \times 10^{-8}$ , and the *d*-TST rate yields  $\sim 2 \times 10^{-8}$ .

As pointed out in Wang et al. (2016), the inclusion of the misreported NIST-database rate to V20 leads to a significantly lower value of  $3 - 4 \times 10^{-9}$  (red solid line in Figure B2). This result highlights the high sensitivity of the manually built chemical network (V12) to this particular reaction, with the quenched CO abundance differing by approximately an order of magnitude between V12 and V20. In contrast, the RMG-generated network shows much less sensitivity: even with the fastest *d*-TST Hidaka rate, the quenched CO value changes by less than a factor of two. This robustness highlights the advantage of RMG's rate-based and more comprehensive network construction over the manually constructed chemical network.

Given the significant role of the Hidaka reaction across the temperature range relevant to Jupiter's deep atmosphere, and its validation by multiple *ab initio* studies, this reaction, at least, should be included in chemical networks using either the *d*-TST (Sanches-Neto et al. 2017) or conventional TST rate (Moses et al. 2011). In this study, we adopt the conventional TST rate from Moses et al. (2011) as the default. Omitting the Hidaka reaction introduces unnecessary uncertainty and can lead to underestimation of the quenched CO abundance, a key diagnostic for constraining Jupiter's deep atmospheric oxygen content.

### 3.2. Constraining the Oxygen Abundance using the 1D Thermochemical Modeling

In this section, we present results from the EPACRIS–1D thermochemical kinetic-transport atmospheric modeling (as described in Section 2.4) and discuss how they can help us constrain the oxygen abundance in Jupiter's deep atmosphere.

#### 3.2.1. $\text{O}/\text{H} = 2.3 \times Z_{\odot}$ scenario

Among the various oxygen abundance scenarios, we first tested the  $2.3 \times Z_{\odot}$  case close to the value of  $2.7 \times Z_{\odot}$  inferred from Juno's microwave radiome-

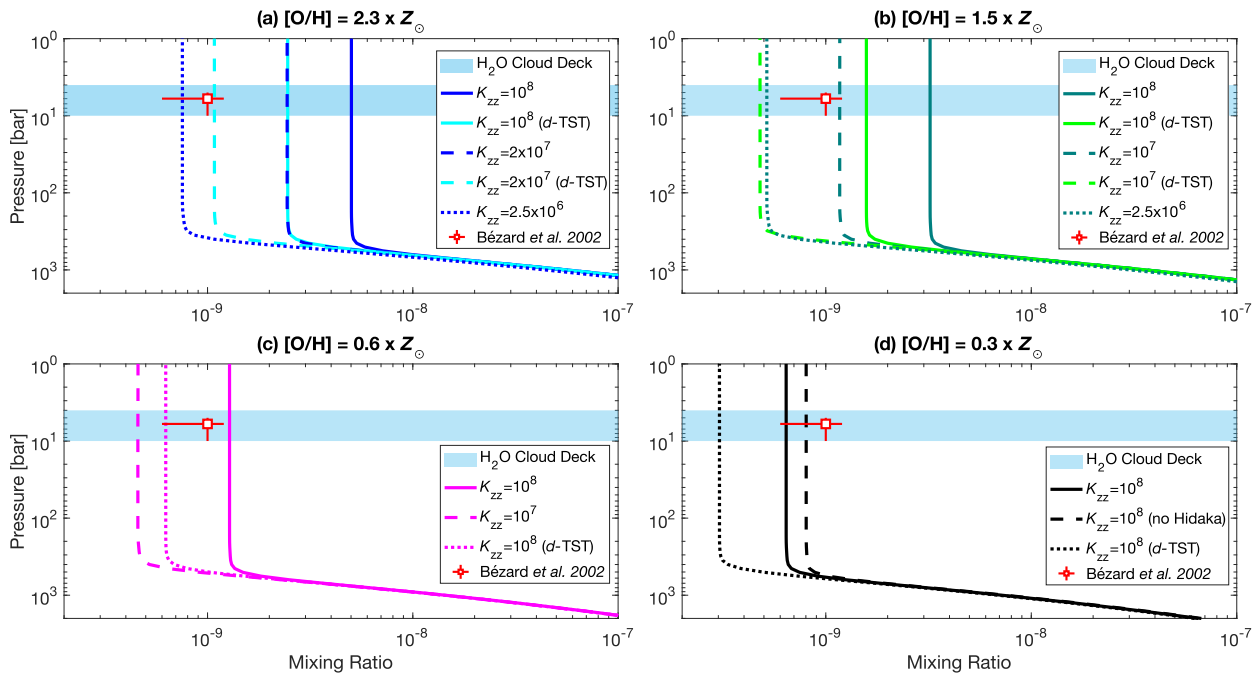


**Figure 2.** Vertical mixing-ratio profiles of carbon monoxide ( $[\text{CO}]/[\text{H}_2]$ ) in Jupiter’s atmosphere for various oxygen abundances O/H (Section 2.1): (a)  $2.3 \times Z_\odot$ , (b)  $1.5 \times Z_\odot$ , (c)  $0.6 \times Z_\odot$ , and (d)  $0.3 \times Z_\odot$ . In each panel, we vary the eddy diffusion coefficient  $K_{zz}$  [ $\text{cm}^2/\text{s}$ ] and adopt the Hidaka reaction rate coefficient from either Moses et al. (2011) (nominal) or Sanches-Neto et al. (2017) (indicated as *d*-TST). Panel (d) additionally shows the CO profile simulated with the Hidaka reaction omitted from the chemical network described in Section 2.3. The red square with error bars indicates the observed upper-tropospheric CO mixing ratio from Bézard et al. (2002), with uncertainties from Bjomaker et al. (2018). The light blue shaded region indicates the water cloud decks between 4 and 10 bars.

ter data (Li et al. 2020). As shown in Figure 2a, using an eddy diffusion coefficient of  $10^8 \text{ cm}^2/\text{s}$ , a commonly adopted value for Jupiter’s deep atmosphere (Visscher et al. 2010; Wang et al. 2015, 2016; Cavalié et al. 2023), our model predicts a CO mixing ratio of  $5 \times 10^{-9}$ . This is almost a factor of five higher than the observed CO mixing ratio value reported by Bézard et al. (2002). Even when using the *d*-TST rate for the Hidaka reaction, which increases CO-to- $\text{CH}_4$  conversion and lowers the CO abundance, the model still overpredicts CO by a factor of about two. To match the observed CO level, the eddy diffusion coefficient must be reduced to  $2.5 \times 10^6 \text{ cm}^2/\text{s}$  when using the nominal Hidaka rate (Moses et al. 2011), or to  $2 \times 10^7 \text{ cm}^2/\text{s}$  when using the *d*-TST rate (Sanches-Neto et al. 2017). However, such low  $K_{zz}$  values, especially below  $\sim 10^6 \text{ cm}^2/\text{s}$ , are likely inconsistent with Jupiter’s observed thermal structure and intrinsic heat flux, which indicate vigorous convection in the deep troposphere, especially if one considers the dry Jupiter case in radiative-convective equilibrium (Stone 1976), where the resulting eddy diffusion coefficient can be as high as  $\sim 10^9 \text{ cm}^2/\text{s}$ .

However, a lower mixing strength is possible according to the 2D hydrodynamic modeling in this work (see Section 3.3 and 3.4). These results suggest that an oxygen abundance of  $2.3 \times Z_\odot$  is too high to reproduce the observed CO quenching behavior in Jupiter’s upper troposphere. Notably, Juno MWR’s latest analysis includes a lower bound of  $1.5 \times Z_\odot$  (Li et al. 2024), allowing us to explore sub- $2 \times Z_\odot$  scenarios.

### 3.2.2. $O/H = 1.5 \times Z_\odot$ scenario

While the  $1.5 \times Z_\odot$  oxygen abundance is introduced here in the context of the EPACRIS–1D thermochemical kinetic-transport modeling, this case was originally tested based on the 2D hydrodynamic modeling result using SNAP, which later identified it as best matching the observed CO mixing ratio (Bézard et al. 2002) (see Section 3.3). As shown in Figure 2b, similar to the  $2.3 \times Z_\odot$  oxygen abundance scenario, using an eddy diffusion coefficient of  $10^8 \text{ [cm}^2/\text{s]}$  results in an overprediction of the CO mixing ratio: approximately a factor of two with the nominal Hidaka reaction rate and about a factor of three even when applying the *d*-TST

rate for Hidaka reaction. To match the observed CO level, the eddy diffusion coefficient needs to fall within approximately  $3 \times 10^6$  to  $1 \times 10^7$  cm<sup>2</sup>/s when using the nominal Hidaka rate (Moses et al. 2011), or between  $1 \times 10^7$  and  $\sim 5 \times 10^7$  cm<sup>2</sup>/s when using the *d*-TST rate (Sanches-Neto et al. 2017). This indicates that a lower  $K_{zz}$  value is required in the deep atmosphere, consistent with the sluggish mixing implied by the presence of a stable radiative layer at depth, as suggested by Cavalié et al. (2023), to reproduce a supersolar oxygen abundance with their chemical network.

### 3.2.3. O/H = 0.6 × $Z_\odot$ scenario

An oxygen abundance of  $0.6 \times Z_\odot$  provides the closest agreement with the observed CO mixing ratio (Bézard et al. 2002) while maintaining the nominal eddy diffusion coefficient of  $10^8$  [cm<sup>2</sup>/s]. As shown in Figure 2, the CO mixing ratio predicted using the nominal Hidaka rate from Moses et al. (2011) slightly exceeds the upper bound of the observational uncertainty (Bézard et al. 2002), whereas using the *d*-TST rate yields a quenched CO mixing ratio near the lower bound. These results suggest that an oxygen abundance of  $0.5\text{--}0.6 \times Z_\odot$  is consistent with the observed CO mixing ratio, though near the edges of the uncertainty range.

Compared to the lower oxygen abundance of  $\sim 0.3 \times Z_\odot$  reported by Cavalié et al. (2023), the present study favors a value roughly twice as high. This discrepancy likely stems from our inclusion of the Hidaka reaction and additional kinetic pathways absent from the V20 network used by Cavalié et al. (2023). Nevertheless, both the current 1D thermochemical modeling using EPACRIS and Cavalié et al. 2023 converge on a sub-solar oxygen abundance in Jupiter's deep atmosphere, lending partial support to Cavalié et al. (2023)'s conclusion regarding sub-solar oxygen levels in Jupiter's troposphere, provided that a deep atmospheric eddy diffusion coefficient of  $10^8$  [cm<sup>2</sup>/s] is assumed. However, this sub-solar value remains significantly lower than the lower bound of  $1.5 \times Z_\odot$  inferred from the latest Juno MWR analysis by Li et al. (2024), suggesting that such low oxygen values are less likely to represent Jupiter's true deep atmospheric composition.

### 3.2.4. O/H = 0.3 × $Z_\odot$ scenario

An oxygen abundance of  $0.3 \times Z_\odot$  was tested based on the previous 1D thermochemical kinetic-

transport modeling by Cavalié et al. (2023), which identified around this value (i.e.,  $0.3 \times$  protosolar or  $0.37 \times Z_\odot$ ) as the best fit for reproducing the observed CO mixing ratio. As shown in Figure 2d, adopting both the nominal eddy diffusion coefficient ( $K_{zz}$ ) of  $10^8$  [cm<sup>2</sup>/s] and the nominal Hidaka rate coefficient (Moses et al. 2011) results in a CO mixing ratio near the lower bound of the observational uncertainty. In contrast, using the *d*-TST rate leads to a predicted CO mixing ratio that falls significantly below the observed range. We also tested the effect of removing the Hidaka reaction from the chemical network, which shifted the quenched CO mixing ratio to  $8 \times 10^{-10}$ , a value that falls within the observed range, including its uncertainty, and is consistent with the result reported by Cavalié et al. (2023).

These results suggest that a  $K_{zz}$  value larger than  $10^8$  [cm<sup>2</sup>/s] is required to match the observed CO mixing ratio when assuming an oxygen abundance of  $0.3 \times Z_\odot$ . This higher  $K_{zz}$  value is less likely the case, since previous studies by Wang et al. (2015, 2016) showed that  $K_{zz}$  decreases from about  $10^8$  [cm<sup>2</sup>/s] near the equator to  $10^7$  [cm<sup>2</sup>/s] at a latitude of 90°. In addition, Bjoraker et al. (2018) constrained an even lower GeH<sub>4</sub> mixing ratio, which implies a required  $K_{zz}$  in the range of  $5 \times 10^6$  to  $10^8$  [cm<sup>2</sup>/s], based on the GeH<sub>4</sub> chemistry modeling by Wang et al. (2016). However, it should be noted that the chemical kinetics for GeH<sub>4</sub> used in Wang et al. (2015) were based on analogies with silicon chemistry, and the actual behavior of germanium under Jovian conditions may differ. Therefore, improving our understanding of germanium kinetics remains an important direction for future study.

Overall, our EPACRIS–1D modeling across a range of O/H and  $K_{zz}$  values favors a best-fitting oxygen abundance between 0.5 and  $0.6 \times Z_\odot$ , with  $K_{zz}$  constrained to values below  $10^8$  [cm<sup>2</sup>/s]. However, if slower mixing is allowed, as suggested by the presence of a deep and stable radiative layer in Cavalié et al. (2023), oxygen abundance as high as 1.5 to even  $2.3 \times Z_\odot$  can match the observed CO mixing ratio (Bézard et al. 2002).

### 3.2.5. CO–CH<sub>4</sub> chemistry in the deep atmosphere of Jupiter and chemical timescale approach

We performed a rate analysis of CO–CH<sub>4</sub> chemistry to understand the CO–CH<sub>4</sub> interconversion pathways in Jupiter's deep atmosphere in detail, as illustrated in Figure 3. Although Figure 3 specifically depicts the reaction pathway scheme for CO

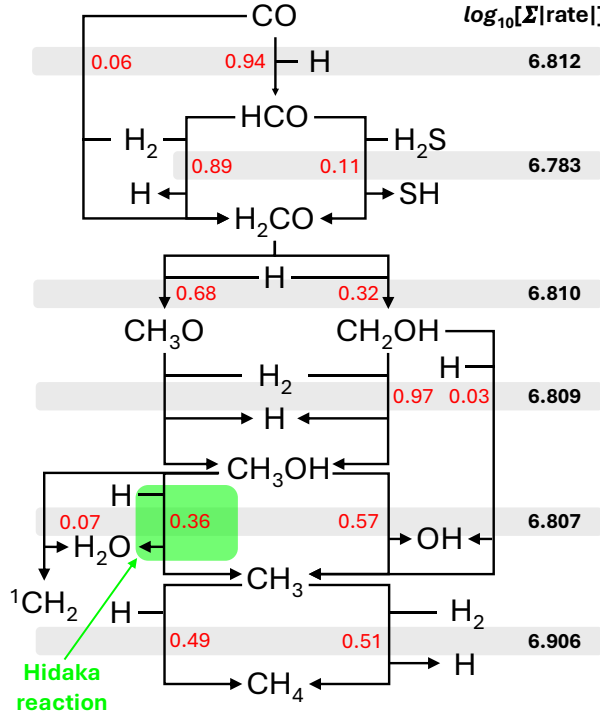


**Figure 3.** Major reaction pathways at the CO quenching point ( $P \sim 505$  bar,  $T \sim 1050$  K) for CO–CH<sub>4</sub> conversion under O/H=1.5 ×  $Z_{\odot}$  and  $K_{zz} = 10^7$  [cm<sup>2</sup>/s]. Red numbers indicate branching ratios for species destruction. For example, 0.06 shows that 6% of CO destruction occurs via the CO+H<sub>2</sub>→H<sub>2</sub>CO reaction, with the remainder (94%) occurring via CO+H→HCO. Therefore, branching ratios sum to 1 (100%). The black numbers on the far right indicate the logarithm of the absolute total rate [molecules/cm<sup>3</sup>/s] of reaction pathways included in the light beige-shaded bars. For example, a value of 6.783 indicates a total HCO destruction rate of  $10^{6.783}$  [molecules/cm<sup>3</sup>/s], representing the combined rates of the reactions HCO+H<sub>2</sub>→H<sub>2</sub>CO+H and HCO+H<sub>2</sub>S→H<sub>2</sub>CO+SH. The green highlighted region identifies the Hidaka reaction, discussed in detail in Section 3.1.

quenching at O/H = 1.5 ×  $Z_{\odot}$  and  $K_{zz} = 10^7$  cm<sup>2</sup>/s, the primary chemical schemes were similar across three other oxygen abundance scenarios shown in Figure 2, differing mainly in each species' total destruction rate.

Initially, 94% of CO converts to HCO via reaction with H radicals, with the remaining 6% directly reacting with H<sub>2</sub> to form H<sub>2</sub>CO. Subsequently, HCO predominantly reacts with H<sub>2</sub> (89%) or alternatively with H<sub>2</sub>S (11%) to yield H<sub>2</sub>CO. H<sub>2</sub>CO primarily interacts with H radicals, generating two isomers: CH<sub>3</sub>O and CH<sub>2</sub>OH. Both isomers mainly react with H<sub>2</sub> to produce CH<sub>3</sub>OH; however,

CH<sub>2</sub>OH also directly forms CH<sub>3</sub> radicals through an additional reaction pathway involving H radicals. Then, 36% of CH<sub>3</sub>OH undergoes the Hidaka reaction, yielding CH<sub>3</sub> and H<sub>2</sub>O. The remainder decomposes via two unimolecular (thermal decomposition) pathways: forming CH<sub>3</sub> + OH (57%) or <sup>1</sup>CH<sub>2</sub> + H<sub>2</sub>O (7%). Finally, CH<sub>3</sub> reacts with either H radicals or H<sub>2</sub> to produce CH<sub>4</sub>, concluding the CO–CH<sub>4</sub> interconversion process.

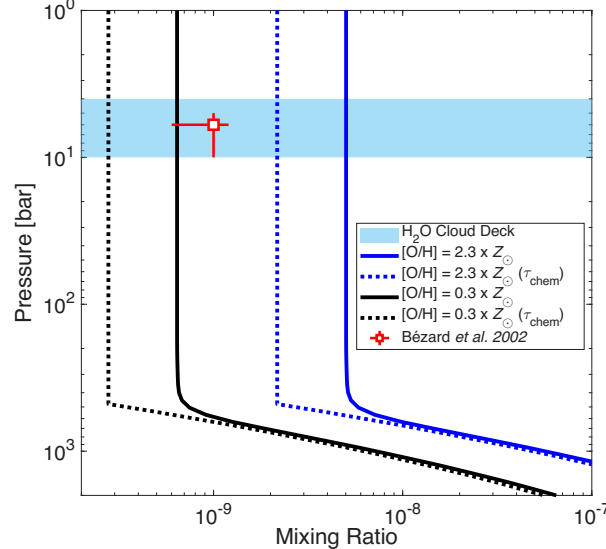


**Figure 4.** Comparison of EPACRIS-1D thermochemical simulations (solid lines; Section 2.4) with the chemical timescale approach approximation using the RMG-generated chemical network (dotted lines; method described in Section 2.7) for two oxygen abundance scenarios: O/H=2.3× $Z_{\odot}$  (blue) and O/H=0.3× $Z_{\odot}$  (black) assuming the same  $K_{zz} = 10^8$  [cm<sup>2</sup>/s]. The red square with error bars indicates the observed upper-tropospheric CO mixing ratio from Bézard et al. (2002), with uncertainties from Bjoraker et al. (2018). The light blue shaded region indicates the water cloud decks between 4 and 10 bars.

One notable point is the absence of a single representative rate-limiting step for the CO-to-CH<sub>4</sub> conversion. Previous studies by Visscher et al. (2010); Visscher & Moses (2011) identified specific reactions, such as CH<sub>3</sub>OH+H→CH<sub>3</sub>O+H<sub>2</sub> or CH<sub>3</sub>OH→CH<sub>3</sub>+OH, as rate-limiting step under Jupiter's atmospheric conditions. Subsequently, Wang et al. (2015) used the rate coefficient for the latter reaction to constrain Jupiter's oxygen abundance within a range of 0.1–0.75 ×  $Z_{\odot}$ . However, our rate analysis (Figure 3) demonstrates that no single reaction dominates. Instead, both the Hidaka reaction and the thermal decomposition of CH<sub>3</sub>OH significantly contribute to CH<sub>3</sub> formation.

Although we employed identical reaction rate coefficients to those used by Visscher & Moses (2011) (Hidaka reaction from Moses et al. (2011); CH<sub>3</sub>OH decomposition from Jasper et al. (2007)), our analysis did not identify a single rate-limiting step, unlike their results. We argue that our finding is more realistic due to the complexity and highly coupled, nonlinear nature of the full chemical reaction network, which makes it unlikely for a single reaction to consistently dominate the rate across all conditions. Consequently, rather than approximating the chemical timescale by focusing on individual reactions (Visscher et al. 2010; Visscher & Moses 2011; Wang et al. 2015), it is more precise to directly compute the characteristic eigenmodes of the Jacobian matrix and their projection to the species of interest (e.g., CO in the current work) at thermal equilibrium across relevant  $T$ - $P$  profiles (e.g., the  $T$ - $P$  profile of Jupiter's atmosphere in the current work). This approach intrinsically captures the nonlinear interplay among all involved reactions and species. To accomplish this, we employed Cantera (Goodwin et al. 2024) (details described in Section 2.7 and Appendix F).

While direct 1D chemical-kinetic transport modeling using EPACRIS is feasible for this study, its computational cost increases significantly with the size of the chemical network, as it scales linearly with the number of reactions and quadratically with the number of species (Schwer et al. 2002). For large chemical networks, such as those developed for predicting polycyclic aromatic hydrocarbon formation, which involve 1594 species and 8924 reactions (Liu et al. 2021a), the chemical timescale approach still remains a computationally practical alternative. This practicality is especially relevant for deep atmospheric studies of planets where thermochemical equilibrium chemistry dominates until it becomes comparable to vertical mixing, making it suitable for Jupiter, Uranus, and Neptune, as well as gas-rich exoplanets (e.g., sub-Neptunes and hot Jupiters). Our comparison of the chemical timescale with the full 1D modeling using EPACRIS (Figure 4) showed that the chemical timescale approach underestimates the CO quenching mixing ratio by approximately 60%. While discrepancies arise due to factors like assumed mixing length ( $L \sim 0.12H$ ; Smith 1998; Visscher et al. 2010) and inherent method limitations (assuming quenching immediately happens at  $\tau_{\text{chem}} = \tau_{\text{mix}}$ ), this deviation remains acceptable in exoplanetary atmospheric studies, where atmospheric retrieval uncer-

tainties within an order of magnitude (1 dex) are typical and considered acceptable. Therefore, the chemical timescale approach may be especially suitable for future studies involving large chemical networks.

### 3.3. Constraining the Oxygen Abundance using the 2D Hydrodynamic Modeling

Compared to Hyder et al. (2025), the current simulations extend to nearly eight times longer run times, allowing for significantly improved convergence. This extended duration is critical because it ensures that the system evolves well beyond transient behavior and reaches a quasi-steady state. As a result, our outcomes provide a more robust and stable representation of the vertical distribution of atmospheric CO over long timescales as opposed to the short-term dynamics that investigated the transport of trace species across the LCL, which was a focus of Hyder et al. (2025). Running the previous Hyder et al. (2025) simulation with a longer timescale would lower the inferred oxygen abundance from about  $2.5 \times Z_{\odot}$  to a value closer to the  $1.5 \times Z_{\odot}$ . This value is still super-solar, so it remains consistent with our current results.

As shown in Figure 5, once the SNAP simulations reach numerical convergence of  $10^{-16}$  (see Figure E5), the vertical mixing ratio profiles of CO stabilize into nearly vertical trajectories across all oxygen abundance scenarios. As part of the convergence criteria, the vertical advection rate is observed to be below machine precision of  $10^{-16}$  (Section 2.5 and Figure E 5) for at least the latter half of the simulations. Among these scenarios, O/H =  $1.5 \times Z_{\odot}$  best matches observational data (Bézard et al. 2002; Bjoraker et al. 2018) (see Figure 5b). Additionally, Figure E4 shows results for O/H =  $1 \times Z_{\odot}$ , where the predicted CO mole fraction remains within observational uncertainty. Thus, our 2D hydrodynamic modeling using SNAP supports a modest supersolar oxygen abundance of  $1-1.5 \times Z_{\odot}$ , consistent with the lower bound of  $1.5 \times Z_{\odot}$  derived from the latest Juno's MWR data analysis(Li et al. 2024). If the true oxygen abundance lies closer to the upper end of the Juno MWR data-inferred range (up to  $8.3 \times Z_{\odot}$ ), which cannot be fit by our current model, this may indicate that additional mechanisms are acting to inhibit CO quenching deeper in the atmosphere. These may include processes beyond CO-CH<sub>4</sub> chemistry and cloud micro-physics, or possibly missing reactions within those frameworks. Clarifying this possibility will require

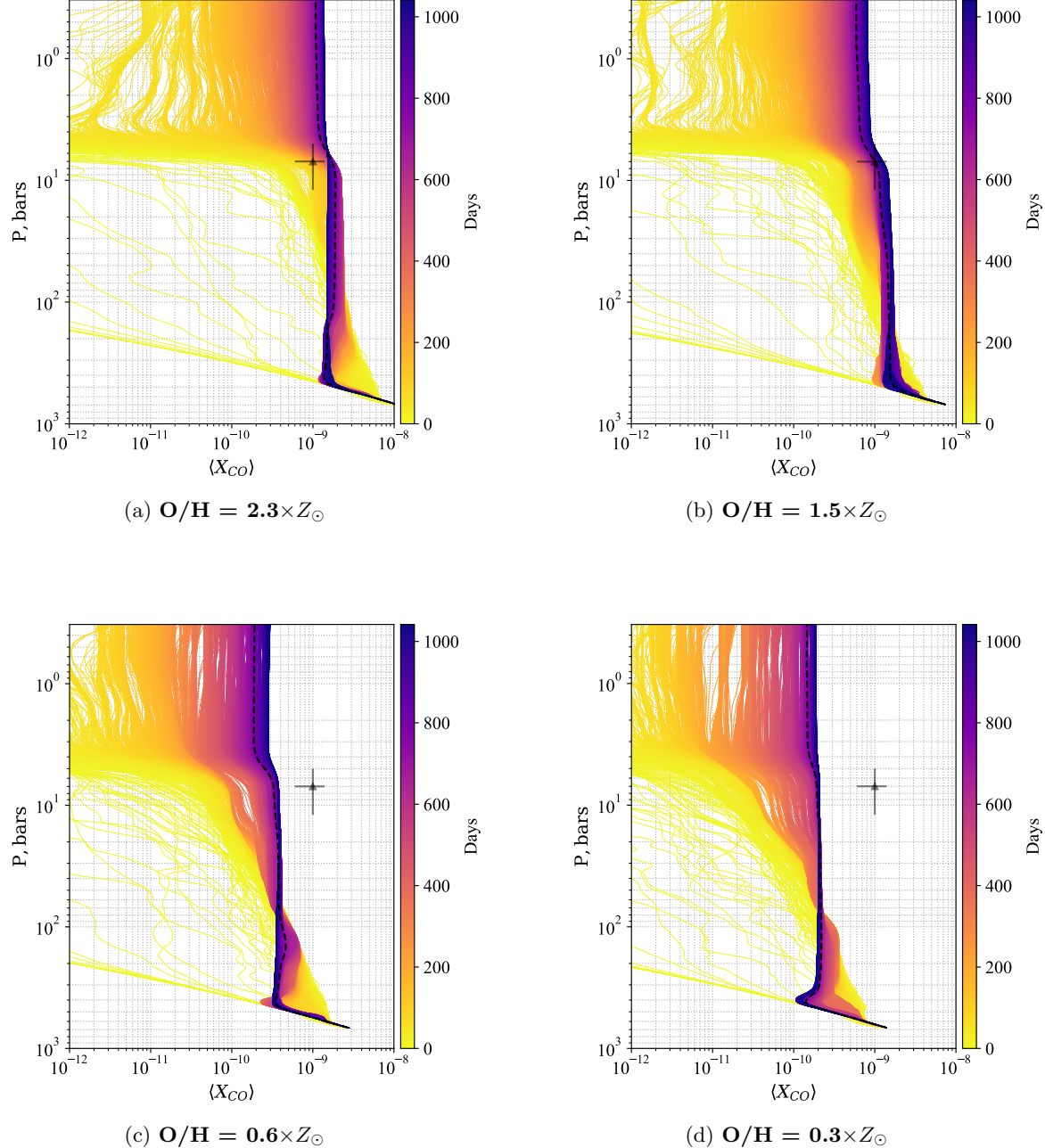


**Figure 5.** The time-dependent behavior of the horizontally averaged CO mole fraction for four different oxygen abundance scenarios using **SNAP-2D** hydrodynamic modeling: (a)  $\text{O}/\text{H} = 2.3 \times Z_{\odot}$ ; (b)  $\text{O}/\text{H} = 1.5 \times Z_{\odot}$ ; (c)  $\text{O}/\text{H} = 0.6 \times Z_{\odot}$ ; and (d)  $\text{O}/\text{H} = 0.3 \times Z_{\odot}$ . The solid gray triangle with error bars indicates the observed upper-tropospheric CO mole fraction from [Bézard et al. \(2002\)](#) and [Bjoraker et al. \(2018\)](#). Dashed lines represent the time-averaged CO mole fraction for each scenario. The underlying eddy diffusion strengths of these cases are not prescribed in the simulations and emerge naturally out of the dynamics. The eddy diffusion profiles are presented in Figure 6.

more precise and extended observations of Jupiter's deep water reservoir.

As discussed in Sections 3.2 and 3.3, assuming O/H =  $1.5 \times Z_{\odot}$  as inferred from our 2D hydrodynamic modeling using **SNAP**, the corresponding one-dimensional thermochemical kinetic-transport modeling yields an estimated eddy diffusion coefficient ( $K_{zz}$ ) in the range of  $3 \times 10^6$  to  $5 \times 10^7$  cm<sup>2</sup>/s, depending on the choice of rate coefficient for the Hidaka reaction (Moses et al. 2011; Sanches-Neto et al. 2017). This value seems out of range compared to the commonly adopted value of  $K_{zz} = 10^8$  [cm<sup>2</sup>/s], originally derived from GeH<sub>4</sub> observations in Jupiter (Bjoraker et al. 1986), and later constrained within  $10^7$ – $10^9$  [cm<sup>2</sup>/s] by Wang et al. (2016), assuming factor-of-five uncertainties in the GeH<sub>4</sub>–GeO chemical kinetics rates. However, a more recent analysis by Bjoraker et al. (2018) reported an average GeH<sub>4</sub> concentration of  $0.35 \pm 0.05$  ppb in Jupiter's Great Red Spot, approximately half the previously reported value ( $0.7 \pm 0.2$  ppb). Using the analogous SiH<sub>4</sub>–SiO chemistry approach from Wang et al. (2016), this updated measurement implies a revised  $K_{zz}$  in the range of  $5 \times 10^6$ – $10^8$  [cm<sup>2</sup>/s], which now aligns well with our 1D model-derived  $K_{zz}$  range of  $3 \times 10^6$ – $5 \times 10^7$  [cm<sup>2</sup>/s]) under the assumption of a  $1.5 \times$  supersolar oxygen abundance.

It should be noted, however, that the analogy between GeH<sub>4</sub>–GeO and SiH<sub>4</sub>–SiO chemical kinetics is imperfect and requires further investigation. A more accurate constraint on  $K_{zz}$  would require updated kinetic data specific to the GeH<sub>4</sub>–GeO system, which is beyond the scope of this study.

### 3.4. Estimating $K_{zz}$ from 2D hydrodynamic modeling using the Quasi Steady-State

Can we derive  $K_{zz}$  from 2D hydrodynamic modeling? Unlike the conventional 1D thermochemical kinetic-transport approach (here using EPACRIS), which often adopts a prescribed  $K_{zz}$  that is not firmly based on physical or chemical principles, 2D hydrodynamic modeling enables a more physics-based derivation. In this framework, the effective eddy diffusion coefficient,  $K_{zz}$ , is not a free parameter but emerges from the underlying fluid dynamics. It depends on several factors, including the distortion of the chemical tracer field, making it a more self-consistent and physically motivated estimate of vertical mixing. Given the widespread use of  $K_{zz}$  in exoplanet atmospheric modeling, this approach offers a powerful framework that enables

more robust constraints on  $K_{zz}$  based on physically grounded dynamics rather than arbitrary assumptions.

As our chemical equilibrium distribution is primarily a function of the vertical coordinate, it can be assumed to be horizontally uniform. Strictly speaking, this is dependent on the latitudinal distribution of water in the planet's atmosphere, whose non-uniformity would lead to additional non-diffusive effects (Zhang & Showman 2018). In this capacity, our CO tracer field is horizontally well-mixed with a vertically varying interconversion time that becomes dominant near the 500 bar pressure region ( $\tau_{\text{chem}} \sim 10^4$  s).

A general solution for the convection-diffusion-reaction equation is not known for arbitrary initial conditions. Historically, estimates of the mixing strength are derived assuming a dry atmosphere with Jupiter's thermal structure and heat flux (e.g., Stone 1976; Flasar 1986). Although these provide a useful constraint on the atmospheric turbulent diffusivity, they do not take into consideration the non-linear advective motions in the atmosphere and inhibitive effects near the cloud layer, which can cause a notable drop in the diffusive strength due to the decreased mass flux across the clouds (Sugiyama et al. 2014). Although  $K_{zz}$  approximates the dominant vertical diffusive component in the context of dry convection, eddy diffusion is generally a tensor with non-analytical solutions for its terms.

Although the full convection–diffusion–reaction equation has no general solution for arbitrary initial and boundary conditions (Kim 2020), we derive an eddy diffusion coefficient from the steady-state conditions of our 2D hydrodynamic simulations using **SNAP**. Using the convection–diffusion equation from Vallis (2017), the eddy diffusion coefficient can be written as

$$\overline{K_{zz}} \sim \left( -\overline{v(z)q(z)} + \int_z \overline{S(z')} dz' \right) \left( \frac{\partial \overline{q}}{\partial z} \right)^{-1}, \quad (4)$$

where  $v(z)$  is the vertical velocity,  $q(z)$  is the CO vertical distribution, and  $S(z')$  is the thermochemical term that approximates the CO production and loss as a function of the pressure and temperature distribution (the integration is performed over a dummy variable,  $z'$ ). The overline indicates a horizontal and temporal average of the specific field. Since the eddy fluxes dominate in the vertical direction,  $\overline{vq} \sim \overline{v'q'}$ , resulting in the conventional relation between the mean tracer gradient distribution

and the vertical eddy flux if the source term is ignored. Equation 4 assumes a steady-state of the system, where  $q(z)$  has stabilized and  $\partial q(z)/\partial z$  is very close to 0 through most of the atmosphere. If one uses the actual steady-state tracer distribution (demarcated by the black dashed lines in Figure 5), equation 4 becomes undefined in specific regions; specifically, the diffusive process is less dominant by the time the tracer field has fully stabilized. We use a mean tracer profile from the final few stages of the simulations that are approaching the steady-state distribution but still allow for the *quasi* steady-state mean eddy diffusivity ( $\bar{K}_{zz}$ ) to be approximated. We present the corresponding  $K_{zz}-P$  profiles for each case shown in Figure 5 in Figure 6.

We note that the eddy diffusivity occasionally becomes negative, which is consistent with the 3D hydrodynamical simulations performed by Zhang & Showman (2018). Depending on the correlation between the vertical velocity field and horizontal tracer fluctuation, the tracer field can be distorted large enough that the derived  $\bar{K}_{zz}$  falls below zero. This occurs for all oxygen enrichment cases as there is a significant non-diffusive contribution that shapes the tracer distribution. The mean horizontal eddy fluxes in our simulations are about 2 orders of magnitude larger than the vertical fluxes.

The interpretation of the diffusivity estimate is made more complicated by the fact that we use a varying CO timescale in contrast to the simplified short- and long-lived interconversion timescales employed by previous GCMs (Zhang & Showman 2018). Thus, our simulations always retain some degree of non-diffusive contributions that shape the tracer distribution, particularly as the mean zonal flow can drastically alter the overall eddy diffusivity along the isobars. The magnitude of the vertical eddy diffusivity in each enrichment case tends to be around the expected range. Although these magnitudes exceed realistic bounds when a purely diffusive treatment is applied (as in equation 4) to regions with non-diffusive dynamics, the overall magnitudes never fall below  $\sim 10^5$  [cm<sup>2</sup>/s] except for the [O/H] = 0.3 case, which falls as low as  $\sim 2 \times 10^4$  [cm<sup>2</sup>/s] due to weakened mixing that is expected in such low humidity systems (Seeley & Wordsworth 2023). Further exploration of the tracer distribution as a function of the vertical and horizontal eddy fluxes will be presented in a 3D model with latitudinal variability (Hyder et al. in prep.).

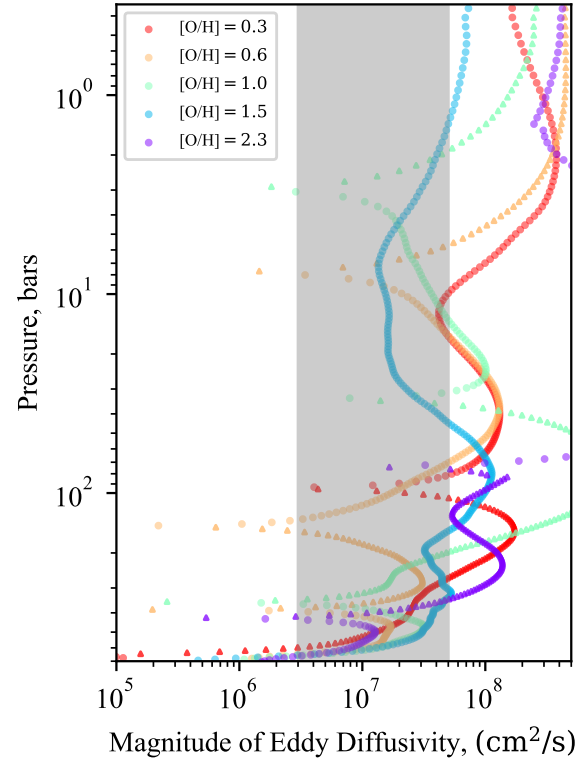


**Figure 6.** The magnitude of the mean eddy diffusion profiles as estimated using equation 4. The profiles are not positive-definite, as is the case within the 1D framework (EPACRIS). The positive values are demarcated by circles, while triangles are used for the negative values. The gray region represents the  $3 \times 10^6$  to  $5 \times 10^7$  [cm<sup>2</sup>/s] range, which aligns with the  $K_{zz}$  values estimated from the EPACRIS-1D modeling under the assumption of O/H = 1.5 to match the observed CO abundance. The negative diffusivity is representative of the non-diffusive effects present in all of our simulations. The profiles occasionally become very large in magnitude as the tracer gradients get closer to zero, signifying a general breakdown of the fully diffusive treatment. The overall magnitudes, however, tend to be consistently within the range of expected vertical eddy coefficients that are estimated from 1D thermochemical modeling using EPACRIS.

However, in general, as shown in Figure 6, this 2D-hydrodynamic modeling-derived  $K_{zz} - P$  aligns well with our EPACRIS-1D modeling constraint on  $K_{zz} - P$  ( $3 \times 10^6$ – $5 \times 10^7$  [cm<sup>2</sup>/s]) assuming a 1.5× supersolar oxygen abundance. This agreement is notable, given that the two modeling frameworks address complementary aspects of the problem. The EPACRIS-1D model captures detailed chemical kinetics but does not fully represent fluid dynamical processes. In contrast, the 2D hydrodynamic model (SNAP) resolves atmospheric motions but re-

lies on simplified chemistry. By coupling these two approaches, our current framework offers a more comprehensive and first-principle grounded method for constraining both chemical and dynamical behavior in (exo)planetary atmospheres.

### 3.5. Discussion of Elevated Jovian C/O Ratio in the Context of Planet Formation and Solar Nebula Chemistry

The current work suggests an O/H=1-1.5×solar abundance (corresponding to an H<sub>2</sub>O abundance of ∼930–1395 ppm), which, when coupled with the firmly established GPMS measurement of Jupiter’s [C/H]=4.0×solar abundance, implies a significantly elevated planetary C/O~2.9 even compared to the recently proposed protosolar ratio (0.73 ± 0.10) by Truong et al. (2024), which is higher than the commonly adopted value of 0.54 (Lodders 2021). Truong et al. (2024) argue that higher solar C/O ratios help reconcile the compositions of large Kuiper Belt Objects (KBOs), such as the Pluto–Charon system, by reducing water ice abundance through increased partitioning of carbon into refractory organics, CO, and CO<sub>2</sub>. Our results might extend this narrative, demonstrating that Jupiter’s formation region was likely far richer in carbon relative to oxygen compared to the broader protosolar nebula, highlighting significant local compositional heterogeneity and radial fractionation within the protoplanetary disk. Such an elevated planetary C/O ratio suggests Jupiter predominantly accreted carbon-rich planetesimals or ices rather than water-rich solids, consistent with the reduced water ice predictions from the higher protosolar C/O scenario suggested by Lodders (2004); Truong et al. (2024). This modeling result reinforces a formation scenario where radial drift (Lunine et al. 2004; Booth et al. 2017), differential condensation (Öberg & Bergin 2016), or selective migration of carbon-rich solids substantially enriched Jupiter’s feeding zone. Together, these insights highlight the complexity and chemical diversity of the early solar nebula, providing essential benchmarks for interpreting compositional diversity within our solar system (which can be extended to Uranus and Neptune) and across exoplanetary systems. Further studies are required to clarify the mechanisms behind the preferential accretion of carbon-rich material, which will enhance our understanding of planetary formation and nebular chemistry.

## 4. CONCLUSIONS

In this work, we have explored Jupiter’s deep atmospheric oxygen abundance by coupling one-dimensional thermochemical kinetic-transport modeling and two-dimensional hydrodynamic modeling. Using a comprehensive and rate-based chemical network generated by the Reaction Mechanism Generator (RMG), we investigated the impact of key chemical pathways, particularly reviewing in detail and emphasizing the significance of the Hidaka reaction, which previous studies have inconsistently or improperly considered.

Our 1D modeling using EPACRIS suggests that an oxygen abundance ranging from approximately 0.5 to 0.6 times solar is most consistent with observational constraints, assuming standard eddy diffusion values ( $K_{zz} \leq 10^8$  [cm<sup>2</sup>/s]). However, such sub-solar oxygen abundances are less likely to represent Jupiter’s true deep atmospheric composition when compared to the latest Juno MWR analysis (Li et al. 2024). This discrepancy might suggest that slower vertical mixing is present, possibly due to stable radiative layers as proposed by Cavalié et al. (2023). Under such conditions, oxygen abundances as high as 2.3 times solar, or even higher, could also be consistent with the observational data.

In contrast, our 2D hydrodynamic simulations using SNAP strongly support a modest supersolar oxygen abundance of approximately 1–1.5 times solar, consistent with the lower bound inferred from the latest Juno MWR analysis (Li et al. 2024). We also introduce a method for deriving Jupiter’s eddy diffusion coefficient ( $K_{zz}$ ) from 2D hydrodynamic modeling using the quasi-steady-state approach. Interestingly, rather than the nominal value of  $K_{zz} = 1 \times 10^8$  cm<sup>2</sup> s<sup>-1</sup>, our results support a revised value of  $K_{zz} \sim 3 \times 10^6$  cm<sup>2</sup> s<sup>-1</sup>, based on the agreement between two independent yet sophisticated approaches—1D chemical–kinetic transport modeling and 2D hydrodynamic modeling. This method has broad applicability to exoplanet atmospheric modeling, where  $K_{zz}$  remains highly uncertain despite its significant influence on atmospheric chemistry.

Our results also imply a notably elevated carbon-to-oxygen (C/O) ratio in Jupiter compared to current protosolar estimates (up to 0.73), suggesting that Jupiter likely accreted predominantly carbon-rich planetesimals or ices (Lodders 2004). This finding underscores the need for further study to

clarify the mechanisms behind the preferential accretion of carbon-rich material during planetary formation, which will significantly inform models of giant planet formation and nebular chemistry.

Ultimately, our integrated modeling approach, which combines detailed thermochemical kinetics with hydrodynamic processes, provides a robust framework for constraining Jupiter's deep atmospheric composition. This methodology not only advances our understanding of Jupiter but also serves as a comprehensive and physically grounded tool for investigating coupled chemical and dynamical processes in (exo)planetary atmospheres.

## ACKNOWLEDGMENTS

The research was carried out at the Jet Propulsion Laboratory, California Institute of Technology, under a contract with the National Aeronautics and

Space Administration (80NM0018D0004). JY was funded by the Caltech-JPL President's and Director's Research and Development Fund, awarded to RH. AH was funded by the NASA Postdoctoral Program (NPP). © 2025. California Institute of Technology. Government sponsorship. acknowledged. The High Performance Computing resources used in this investigation were provided by funding from the JPL Information and Technology Solutions Directorate.

## AUTHOR CONTRIBUTIONS

JY conceptualized and led the project. JY, AH, and RH jointly designed the study. JY led the writing of the manuscript. JY conducted and analyzed 1D thermochemical kinetic-transport modeling (**EPACRIS**). AH conducted and analyzed 2D hydrodynamic modeling (**SNAP**). All authors contributed to the writing and revision of the manuscript.

## APPENDIX

### A. ELEMENTAL PARAMETERIZATION OF JUPITER'S ATMOSPHERE

This appendix demonstrates a detailed description of the O/H variation mentioned in Section 2.1 in the form of Table A 1 for easier comparison with previous studies.

### B. $T - P$ & $K_{zz}$ PROFILES

Figure A1 shows the  $T - P$  and  $K_{zz}$  profiles adopted in the current study.

### C. CHEMICAL NETWORKS COMPARISON

Figure C 2 shows comparisons among vertical mole fraction ( $X_{CO} = [CO]/n$ , where  $n$  is total number density of the atmosphere [molecules/cm<sup>3</sup>]) profiles of CO in Jupiter's troposphere computed under identical conditions ( $K_{zz} = 10^9$  cm<sup>2</sup>/s; He, C, N, and S abundances described in Section 2.1; O/H=7× $Z_{\odot}$ ), as shown in Fig. 17 of Wang et al. (2016), but using various chemical networks.

### D. CHEMICAL TIMESCALE FITTINGS

Table D2 summarizes the conditions for the 10 datasets used for the empirical fitting of the chemical timescale described in Section 2.6. Figure D3 presents the details of the fitting process and compares the resulting empirical timescale with that

from the previous study by Wang et al. (2015). Note that the chemical timescale derived by Wang et al. (2015) is based on the V12 chemical network developed by Venot et al. (2012).

### E. SUPPLEMENTARY MATERIALS FOR SNAP SIMULATIONS

Figure E4 shows the time-dependent behavior of the horizontally averaged CO mole fraction for O/H=1.0× $Z_{\odot}$ . Figure E5 shows the mean tracer rate of change as the balance between hydrodynamical turbulent transport and chemical production and loss, which is used to determine the convergence criteria of SNAP used in this work.

**Table A 1.** Elemental composition profiles used in this study to model Jupiter's atmosphere

O/H enrichment compared to present-day solar abundance ( $Z_{\odot}$ )					
$E$	0.3×	0.6×	1.0×	1.5×	2.3×
<b>H</b>	0.925735	0.925597	0.925413	0.925183	0.924806
<b>He (<math>0.9 \times Z_{\odot}</math>)<sup>a</sup></b>	0.072670	0.072659	0.072645	0.072627	0.072597
<b>C (<math>4.0 \times Z_{\odot}</math>)<sup>b</sup></b>	0.001097	0.001097	0.001097	0.001096	0.001096
<b>N (<math>4.7 \times Z_{\odot}</math>)<sup>c</sup></b>	0.000307	0.000307	0.000307	0.000307	0.000307
<b>O<sup>d</sup></b>	0.000149	0.000298	0.000497	0.000745	0.001153
<b>S (<math>3.2 \times Z_{\odot}</math>)<sup>e</sup></b>	0.000041	0.000041	0.000041	0.000041	0.000041
<b>C/O</b>	7.36	3.68	2.21	1.47	0.95

NOTE—<sup>a</sup>  $[\text{He}]/[\text{H}_2]=0.157$  was taken from Wang et al. (2016). Thus  $\text{He}/\text{H} \sim 7.85 \times 10^{-2}$

<sup>b</sup>  $[\text{CH}_4]/[\text{H}_2]=2.37 \times 10^{-3}$  was taken from Wang et al. (2016). Thus  $\text{C}/\text{H} \sim 1.19 \times 10^{-3}$

<sup>c</sup>  $[\text{NH}_3]/[\text{H}_2]=6.64 \times 10^{-4}$  was taken from Wang et al. (2016). Thus  $\text{N}/\text{H} \sim 3.32 \times 10^{-4}$

<sup>d</sup> O/H was varied by  $A(E)=8.73+\log_{10}E$ , where  $E$  is an enrichment factor for oxygen. Thus  $\text{O}/\text{H} \sim 10^{A(E)-12}$ .

<sup>e</sup>  $[\text{H}_2\text{S}]/[\text{H}_2]=8.90 \times 10^{-5}$  was taken from Wang et al. (2016). Thus  $\text{S}/\text{H} \sim 4.45 \times 10^{-5}$

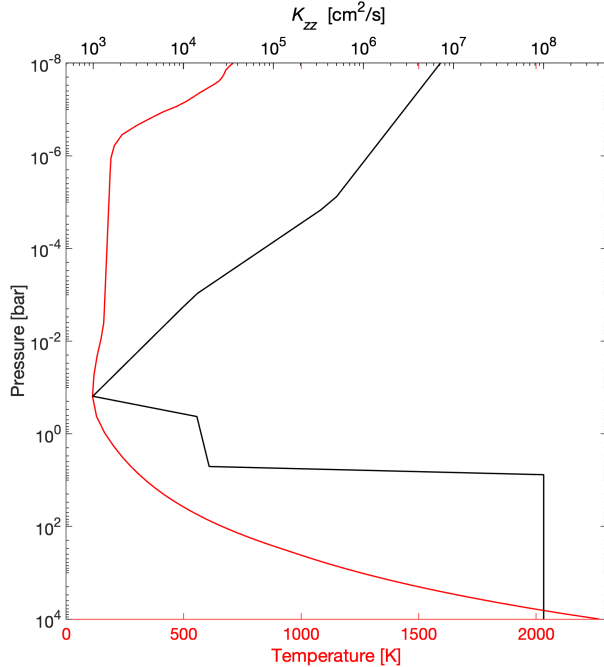


**Figure B 1.** The temperature-pressure ( $T$ - $P$ ) and eddy diffusion coefficient ( $K_{zz}$ ) profiles adopted in the current study. The red solid line represents the  $T$ - $P$  profile from Seiff et al. (1998); Simon-Miller et al. (2006), while the black solid line shows the  $K_{zz}$  profile from Moses et al. (2005). In this work, the deep atmospheric  $K_{zz}$  value (uniform at pressures  $P \gtrsim 8$  bar) has been varied from  $5 \times 10^6$  to  $10^9$   $\text{cm}^2/\text{s}$ , with a nominal value of  $10^8$   $\text{cm}^2/\text{s}$  shown in this figure.

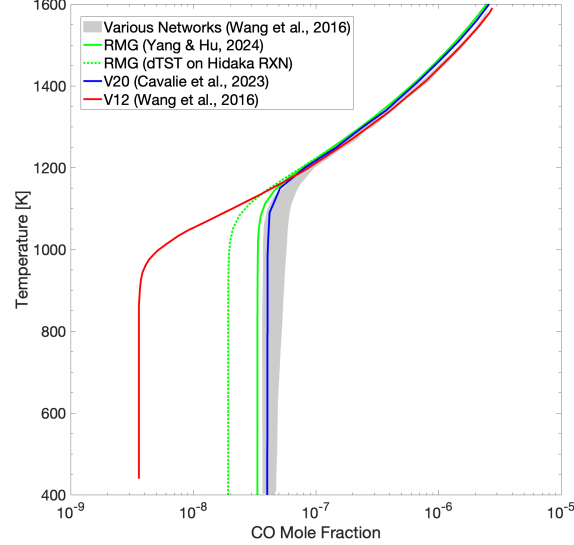


**Figure C 2.** Vertical CO mole fraction profiles ( $X_{\text{CO}}$ ) in Jupiter's troposphere were computed under identical conditions ( $K_{zz} = 10^9$  [ $\text{cm}^2/\text{s}$ ]; O/H =  $7 \times Z_{\odot}$ ; He, C, N, S as in Section 2.1), using various chemical networks. The RMG network from this study (green), V20 network (Venot et al. 2020) (blue), and V12 network (Venot et al. 2012) (red) show close agreement down to  $\sim 1200$  K, below which vertical mixing dominates. The green dotted line shows the RMG network with the Hidaka reaction rate updated from Moses et al. (2011) to the dTST value from Sanches-Neto et al. (2017). The gray shaded region reflects the range of network predictions in Wang et al. (2016). While overall differences are modest, the RMG network predicts slightly more efficient CO-to-CH<sub>4</sub> conversion than V20 and earlier networks under these oxygen-rich conditions.

**Table D 2.** Conditions for the 10 datasets used in the empirical fitting of the chemical timescale in this study

O/H	$K_{zz}$ [cm <sup>2</sup> /s]	[CO] <sup>a</sup>	$\tau_{CO}$ [s]
$0.3 \times Z_{\odot}$ <sup>b</sup>	$1 \times 10^8$	$6.41 \times 10^{-10}$	$2.30 \times 10^5$
$0.3 \times Z_{\odot}$	$1 \times 10^9$	$1.67 \times 10^{-9}$	$2.56 \times 10^4$
$1 \times Z_{\odot}$	$1 \times 10^8$	$2.10 \times 10^{-9}$	$2.15 \times 10^5$
$1.5 \times Z_{\odot}$	$1 \times 10^8$	$3.22 \times 10^{-9}$	$2.26 \times 10^5$
$2.3 \times Z_{\odot}$	$5 \times 10^6$	$1.53 \times 10^{-9}$	$3.75 \times 10^6$
$2.3 \times Z_{\odot}$	$2 \times 10^7$	$2.44 \times 10^{-9}$	$9.96 \times 10^5$
$2.3 \times Z_{\odot}$	$1 \times 10^8$	$5.20 \times 10^{-9}$	$2.24 \times 10^5$
$2.3 \times Z_{\odot}$	$1 \times 10^9$	$1.31 \times 10^{-8}$	$2.50 \times 10^4$
$4 \times Z_{\odot}$	$1 \times 10^8$	$8.51 \times 10^{-9}$	$2.19 \times 10^5$
$7 \times Z_{\odot}$	$1 \times 10^9$	$3.90 \times 10^{-8}$	$2.35 \times 10^4$

<sup>a</sup>Quenched CO mixing ratio

<sup>b</sup>Solar metallicity

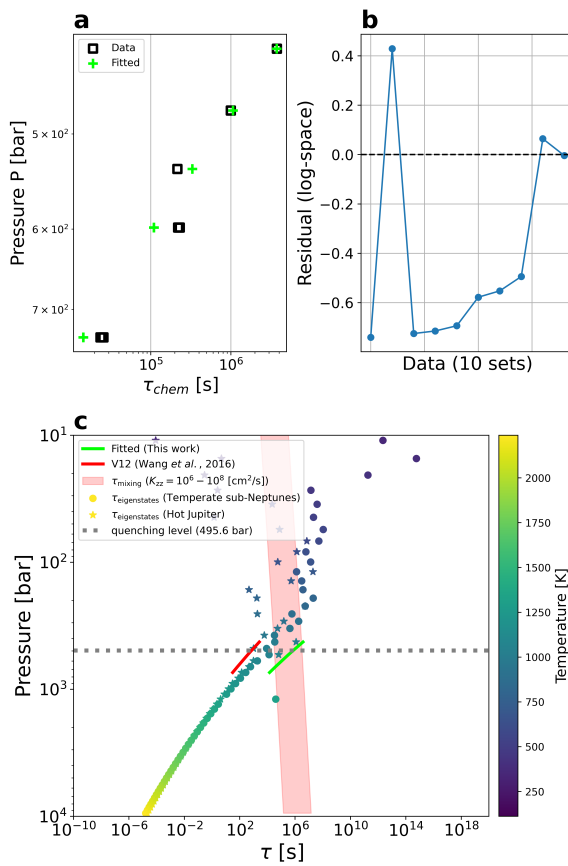


**Figure D 3.** (a) Comparison between the thermochemistry-diffusion model derived data points of  $\tau_{chem}$  described in Section 2.6 (black open squares) versus the fitted points (green cross symbols); (b) Residuals in logspace between the data points and fitted points; (c) Comparison among various chemical timescales of CO ( $\tau_{chem}$ ). The red solid line refers to the derived chemical timescale used in Wang et al. (2015), The green solid line refers to the fitted chemical timescale in this work as described in Section 2.6; The stars refer to the chemical timescale directly calculated under thermochemical equilibrium using the chemical network for the hot Jupiter chemistry used in Yang & Hu (2024a), while the circles refer to the chemical timescale directly calculated under thermochemical equilibrium using the chemical network for the temperate sub-Neptune chemistry used in Yang & Hu (2024b) (see Section 2.7 and Section F). The chemical timescales derived from the two networks are nearly identical at temperatures above 1500 K. Note that the same chemical network is used for the green solid line and circles, but the green solid line was fitted using the method following Wang et al. (2015) whose method is described in Section 2.6, while the circles are directly calculated assuming thermochemical equilibrium using Cantera (Goodwin et al. 2024) and `scipy.linalg.eig` (Virtanen et al. 2020) as described in Section 2.7 and Section F.

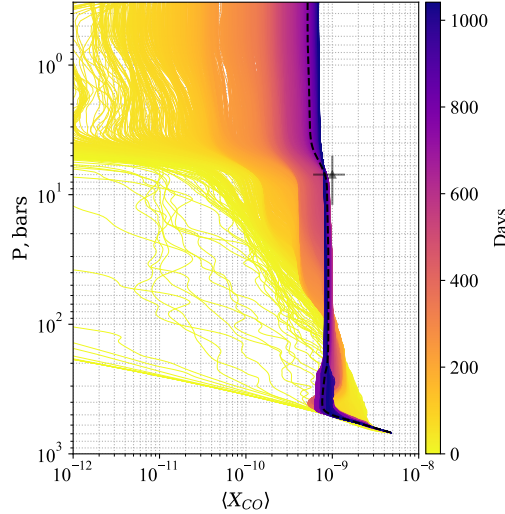


**Figure E 4.** The time-dependent behavior of the horizontally averaged CO mole fraction for  $\text{O/H}=1.0\times Z_\odot$ . The solid gray triangle with error bars indicates the observed upper-tropospheric CO mole fraction from Bézard et al. (2002) and Bjaraker et al. (2018). Dashed line represents the time-averaged CO mole fraction for the  $\text{O/H}=1.0\times Z_\odot$  scenario.

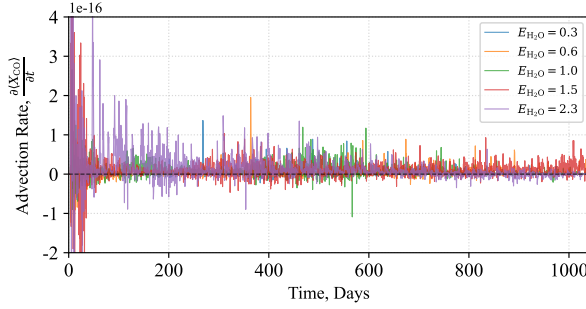


**Figure E 5.** The mean tracer rate of change as the balance between hydrodynamical turbulent transport and chemical production and loss is achieved. By  $\sim 600$  days, the variation is consistently below machine precision ( $10^{-16}$ ), suggestive of a chemical-diffusive steady-state.

## F. CHEMICAL TIMESCALE APPROXIMATION VIA JACOBIAN EIGENMODES DECOMPOSITION

To assess the characteristic chemical timescales of species in Jupiter's deep atmosphere, we built the Jacobian matrix of the chemical system as follows. First, we define the mole fraction column vector

$$\mathbf{X} = (X_1, X_2, \dots, X_N)^T, \quad (\text{F1})$$

where  $X_i$  is the mole fraction of species  $i$  at the given chemical system.  $N$  is the total number of species in the chemical system of interest ( $N=89$  for the chemical network built for the temperate sub-Neptune atmospheric simulation in Yang & Hu (2024b), and  $N=106$  for the chemical network built for the hot Jupiter atmospheric simulation in Yang & Hu (2024a), as shown in Figure D3). This mole fraction column vector  $\mathbf{X}$  evolves according to

$$\frac{d\mathbf{X}}{dt} = \mathbf{f}(\mathbf{X}, T, P) \quad (\text{F2})$$

at the given temperature  $T$  [K] and pressure  $P$  [Pa], where  $\mathbf{f}$  denotes the vector of net production rates normalized by the total concentration, which we calculate using Cantera's `Kinetics.net_production_rates` (Goodwin et al. 2024). At around chemical equilibrium, denoted by  $\mathbf{X}_{\text{eq}}$  with  $\mathbf{f}(\mathbf{X}_{\text{eq}}) = 0$ , we define a perturbation  $\delta\mathbf{X} = \mathbf{X} - \mathbf{X}_{\text{eq}}$ . Assuming locally linearized dynamics around chemical equilibrium,

$$\frac{d\mathbf{X}}{dt} = \frac{d}{dt}(\mathbf{X}_{\text{eq}} + \delta\mathbf{X}) = \frac{d(\delta\mathbf{X})}{dt} \sim \mathbf{J} \cdot \delta\mathbf{X} \quad (\text{F3})$$

where the Jacobian matrix element is

$$J_{ij} = \left. \frac{\partial f_i}{\partial X_j} \right|_{X=X_{\text{eq}}} \quad (\text{F4})$$

Numerically, we compute  $J$  using central finite differences:

$$J_{ij} \sim \frac{f_i(X_j + \Delta) - f_i(X_j - \Delta)}{2\Delta} \quad (\text{F5})$$

where  $\Delta$  is the perturbation of the mole fraction of species  $j$  (i.e.,  $X_j$ ). We set this  $\Delta = 10^{-8}$  for CO analysis. The characteristic modes of the system is given by the eigenvalue problem:

$$\mathbf{J} \cdot \mathbf{v}_k = \lambda_k \cdot \mathbf{v}_k, \quad (\text{F6})$$

$$\mathbf{w}_k^T \cdot \mathbf{J} = \lambda_k \cdot \mathbf{w}_k^T \quad (\text{F7})$$

where  $\mathbf{v}_k$  and  $\mathbf{w}_k^T$  are right and left eigenvectors, respectively, corresponding to  $\lambda_k$ . We used `scipy.linalg.eig` (Virtanen et al. 2020) to compute these eigenvectors and corresponding eigenvalues of the system. Eigenvalues with negative real parts ( $\Re(\lambda_k) < 0$ ) represent decaying modes, with characteristic timescales

$$\tau_k = -\frac{1}{\Re(\lambda_k)} \quad (\text{F8})$$

To connect these modes to the chemical timescale of a specific species (CO in this study), we examined the left eigenvectors, which quantify how perturbations in each species project onto each mode. For a given target species index  $k_{\text{CO}}$ , the row of the left eigenvector matrix provides the projection of CO participation onto every eigenmode. Among the decaying modes (i.e.,  $\Re(\lambda_k) < 0$ ), we choose the  $\Re(\lambda_k)$  in which CO has the largest magnitude of participation (i.e., the mode for which  $\mathbf{w}_k^T$  has the maximum value). The results are shown in Figure D3 for the two chemical networks (hot Jupiter chemical, shown with stars: temperate sub-Neptune, shown with circles) compared with empirical fittings from this work and from Wang et al. (2015).

## REFERENCES

- Asplund, M., Grevesse, N., Sauval, A. J., & Scott, P. 2009, Annual review of astronomy and astrophysics, 47, 481
- Atreya, S., Donahue, T., & Festou, M. 1981, Astrophysical Journal, Part 2-Letters to the Editor, vol. 247, July 1, 1981, p. L43-L47. NASA-supported research., 247, L43
- Benneke, B., Roy, P.-A., Coulombe, L.-P., et al. 2024, arXiv preprint arXiv:2403.03325
- Bézard, B., Lellouch, E., Strobel, D., Maillard, J.-P., & Drossart, P. 2002, Icarus, 159, 95
- Bjoraker, G. L., Larson, H. P., & Kunde, V. G. 1986, Icarus, 66, 579,  
doi: [https://doi.org/10.1016/0019-1035\(86\)90093-X](https://doi.org/10.1016/0019-1035(86)90093-X)
- Bjoraker, G. L., Wong, M. H., de Pater, I., et al. 2018, AJ, 156, 101

- Booth, R. A., Clarke, C. J., Madhusudhan, N., & Ille, J. D. 2017, Monthly Notices of the Royal Astronomical Society, 469, 3994
- Carvalho, E., Barauna, A. N., Machado, F. B., & Roberto-Neto, O. 2008, Chemical Physics Letters, 463, 33
- Carvalho-Silva, V. H., Aquilanti, V., de Oliveira, H. C., & Mundim, K. C. 2017, Journal of computational chemistry, 38, 178
- Cavalié, T., Lunine, J., & Mousis, O. 2023, Nat. Astron., 7, 678
- Chen, D., Wang, K., & Wang, H. 2017, Combustion and Flame, 186, 208
- Drossart, P., Fouchet, T., Crovisier, J., et al. 1999, in The Universe as seen by ISO, Vol. 427, 169
- Drossart, P., Sicardy, B., Roques, F., et al. 2000, in AAS/Division for Planetary Sciences Meeting Abstracts# 32, Vol. 32, 12–09
- Edgington, S., Atreya, S., Trafton, L., et al. 1999, Icarus, 142, 342
- Flasar, F. 1986, Icarus, 65, 280, doi: [https://doi.org/10.1016/0019-1035\(86\)90140-5](https://doi.org/10.1016/0019-1035(86)90140-5)
- Gao, C. W., Allen, J. W., Green, W. H., & West, R. H. 2016, Comput. Phys. Commun., 203, 212, doi: [10.1016/j.cpc.2016.02.013](https://doi.org/10.1016/j.cpc.2016.02.013)
- Goodwin, D. G., Moffat, H. K., Schoegl, I., Speth, R. L., & Weber, B. W. 2024, Cantera: An Object-oriented Software Toolkit for Chemical Kinetics, Thermodynamics, and Transport Processes, 3.1.0, doi: [10.5281/zenodo.14455267](https://doi.org/10.5281/zenodo.14455267)
- Grassi, D., Adriani, A., Mura, A., et al. 2020, Journal of Geophysical Research (Planets), 125, e06206, doi: [10.1029/2019JE006206](https://doi.org/10.1029/2019JE006206)
- Hidaka, Y., Oki, T., Kawano, H., & Higashihara, T. 1989, The Journal of Physical Chemistry, 93, 7134
- Hoyermann, K., Sievert, R., & Wagner, H. G. 1981, Berichte der Bunsengesellschaft für physikalische Chemie, 85, 149
- Hu, R., Bello-Arufe, A., Tokadjian, A., et al. 2025, arXiv preprint arXiv:2507.12622
- Hyder, A., Ge, H., Li, C., & Orton, G. in prep.
- Hyder, A., Li, C., Chanover, N., & Bjoraker, G. 2025, Nature Astronomy, 9, 211
- Jasper, A. W., Klippenstein, S. J., Harding, L. B., & Ruscic, B. 2007, The Journal of Physical Chemistry A, 111, 3932
- Johnson, M. S., Dong, X., Grinberg Dana, A., et al. 2022, J. Chem. Inf. Model., 62, 4906, doi: [10.1021/acs.jcim.2c00965](https://doi.org/10.1021/acs.jcim.2c00965)
- Kerkeni, B., & Clary, D. C. 2004, The Journal of chemical physics, 121, 6809
- Kim, A. S. 2020, Scientific Reports, 10, 8040, doi: [10.1038/s41598-020-63982-w](https://doi.org/10.1038/s41598-020-63982-w)
- Lara, L.-M., Bézard, B., Griffith, C. A., Lacy, J. H., & Owen, T. 1998, Icarus, 131, 317
- Lellouch, E., Bézard, B., Moses, J. I., et al. 2002, Icarus, 159, 112
- Lendvay, G., Bérçés, T., & Márta, F. 1997, The Journal of Physical Chemistry A, 101, 1588
- Li, C., & Chen, X. 2019, Astrophys. J. Suppl. Ser., 240, 37, doi: [10.3847/1538-4365/aafdaa](https://doi.org/10.3847/1538-4365/aafdaa)
- Li, C., Ingersoll, A., Bolton, S., et al. 2020, Nat. Astron., 4, 609
- Li, C., Allison, M., Atreya, S., et al. 2024, Icarus, 414, 116028, doi: <https://doi.org/10.1016/j.icarus.2024.116028>
- Li, S., & Williams, F. 1996, Symposium (International) on Combustion, 26, 1017
- Liu, M., Chu, T.-C., Jocher, A., et al. 2021a, International Journal of Chemical Kinetics, 53, 27
- Liu, M., Grinberg Dana, A., Johnson, M. S., et al. 2021b, Journal of Chemical Information and Modeling, 61, 2686
- Lodders, K. 2004, The Astrophysical Journal, 611, 587
- . 2021, Space Sci. Rev., 217, 44
- Lunine, J. I., Coradini, A., Gautier, D., Owen, T. C., & Wuchterl, G. 2004, Jupiter. The planet, satellites and magnetosphere, 1, 19
- Manion, J., Huie, R., Levin, R., et al. 2020, NIST Chemical Kinetics Database—Standard Reference Database 17, Version 7.0 (Web Version), Release 1.6. 8, Data Version 2017.07
- Meana-Pañeda, R., Truhlar, D. G., & Fernández-Ramos, A. 2011, The Journal of chemical physics, 134
- Moreno, R., Marten, A., Matthews, H., & Biraud, Y. 2003, Planetary and Space Science, 51, 591
- Moses, J. I. 2014, Philosophical Transactions of the Royal Society A: Mathematical, Physical and Engineering Sciences, 372, 20130073
- Moses, J. I., Fouchet, T., Bézard, B., et al. 2005, Journal of Geophysical Research: Planets, 110
- Moses, J. I., Visscher, C., Fortney, J. J., et al. 2011, The Astrophysical Journal, 737, 15
- Mousis, O., Ronnet, T., & Lunine, J. I. 2019, The Astrophysical Journal, 875, 9

- National Academies of Sciences, Engineering, and Medicine. 2023, *Origins, Worlds, and Life: A Decadal Strategy for Planetary Science and Astrobiology 2023-2032* (Washington, DC: The National Academies Press), doi: [10.17226/26522](https://doi.org/10.17226/26522)
- Niemann, H., Atreya, S., Carignan, G., et al. 1998, *J. Geophys. Res. Planets*, 103, 22831
- Öberg, K. I., & Bergin, E. A. 2016, *The Astrophysical Journal Letters*, 831, L19
- Öberg, K. I., Murray-Clay, R., & Bergin, E. A. 2011, *The Astrophysical Journal Letters*, 743, L16
- Prinn, R. G., & Barshay, S. S. 1977, *Science*, 198, 1031
- Sanches-Neto, F. O., Coutinho, N. D., & Carvalho-Silva, V. H. 2017, *Physical Chemistry Chemical Physics*, 19, 24467
- Schwer, D. A., Tolsma, J. E., Green Jr, W. H., & Barton, P. I. 2002, *Combustion and Flame*, 128, 270
- Seeley, J. T., & Wordsworth, R. D. 2023, *PSJ*, 4, 34, doi: [10.3847/PSJ/acb0cb](https://doi.org/10.3847/PSJ/acb0cb)
- Seiff, A., Kirk, D. B., Knight, T. C., et al. 1998, *J. Geophys. Res. Planets*, 103, 22857
- Silva, V. H., Aquilanti, V., de Oliveira, H. C., & Mundim, K. C. 2013, *Chemical Physics Letters*, 590, 201
- Simon-Miller, A. A., Conrath, B. J., Gierasch, P. J., et al. 2006, *Icarus*, 180, 98
- Smith, M. D. 1998, *Icarus*, 132, 176
- Stone, P. H. 1976, in *IAU Colloquium 30: Jupiter: Studies of the Interior, Atmosphere, Magnetosphere and Satellites*, ed. T. Gehrels & S. Matthews, 586–618
- Sugiyama, K., Nakajima, K., Odaka, M., Kuramoto, K., & Hayashi, Y. Y. 2014, *Icarus*, 229, 71, doi: [10.1016/j.icarus.2013.10.016](https://doi.org/10.1016/j.icarus.2013.10.016)
- Truong, N., Glein, C. R., & Lunine, J. I. 2024, *ApJ*, 976, 14, doi: [10.3847/1538-4357/ad7a65](https://doi.org/10.3847/1538-4357/ad7a65)
- Vallis, G. K. 2017, *Atmospheric and Oceanic Fluid Dynamics: Fundamentals and Large-Scale Circulation*, doi: [10.1017/9781107588417](https://doi.org/10.1017/9781107588417)
- Venot, O., Cavalié, T., Bounaceur, R., et al. 2020, *A&A*, 634, A78
- Venot, O., Hébrard, E., Agúndez, M., et al. 2012, *A&A*, 546, A43
- Vervack Jr, R. J., Sandel, B. R., Gladstone, G. R., McConnell, J. C., & Parkinson, C. D. 1995, *Icarus*, 114, 163
- Virtanen, P., Gommers, R., Oliphant, T. E., et al. 2020, *Nature Methods*, 17, 261, doi: [10.1038/s41592-019-0686-2](https://doi.org/10.1038/s41592-019-0686-2)
- Visscher, C., & Moses, J. I. 2011, *The Astrophysical Journal*, 738, 72
- Visscher, C., Moses, J. I., & Saslow, S. A. 2010, *Icarus*, 209, 602
- Wang, D., Gierasch, P. J., Lunine, J. I., & Mousis, O. 2015, *Icarus*, 250, 154
- Wang, D., Lunine, J. I., & Mousis, O. 2016, *Icarus*, 276, 21
- Wong, M. H., Mahaffy, P. R., Atreya, S. K., Niemann, H. B., & Owen, T. C. 2004, *Icarus*, 171, 153
- Yang, J. 2025, RMG-generated Chemical Network for H<sub>2</sub>O-rich atmospheres (Yang and Hu, 2024), Zenodo, doi: [10.5281/zenodo.16750016](https://doi.org/10.5281/zenodo.16750016)
- Yang, J., & Hu, R. 2024a, *ApJ*, 966, 189
- . 2024b, *ApJL*, 971, L48
- Yelle, R. V., Young, L. A., Vervack Jr, R. J., et al. 1996, *Journal of Geophysical Research: Planets*, 101, 2149
- Zahnle, K. J., & Marley, M. S. 2014, *The Astrophysical Journal*, 797, 41
- Zhang, X., & Showman, A. P. 2018, *ApJ*, 866, 1, doi: [10.3847/1538-4357/aada85](https://doi.org/10.3847/1538-4357/aada85)